
Electronic Thesis and Dissertation Repository

11-15-2023 2:30 PM

Revealing the Core Dynamics of Vesta: Insights from Experimental Investigations of Electrical Resistivity and Thermal Conductivity

Oluwasanmi A. Orole Mr, *Western University*

Supervisor: Secco, Richard A., *The University of Western Ontario*

Co-Supervisor: Yong, Wenjun, *The University of Western Ontario*

A thesis submitted in partial fulfillment of the requirements for the Master of Science degree in Geophysics

© Oluwasanmi A. Orole Mr 2023

Follow this and additional works at: <https://ir.lib.uwo.ca/etd>



Part of the [Geophysics and Seismology Commons](#)

Recommended Citation

Orole, Oluwasanmi A. Mr, "Revealing the Core Dynamics of Vesta: Insights from Experimental Investigations of Electrical Resistivity and Thermal Conductivity" (2023). *Electronic Thesis and Dissertation Repository*. 9784.

<https://ir.lib.uwo.ca/etd/9784>

This Dissertation/Thesis is brought to you for free and open access by Scholarship@Western. It has been accepted for inclusion in Electronic Thesis and Dissertation Repository by an authorized administrator of Scholarship@Western. For more information, please contact wlsadmin@uwo.ca.

Abstract

Insights from high pressure and temperature experiments involving in-situ measurements of the electrical resistivity of Fe-5wt%Ni at temperatures of up to 2000 K, under pressures of 2-5 GPa in a 1000-ton cubic-anvil press have been used to reveal Vesta's core dynamics. The Wiedemann–Franz law was used to calculate the thermal conductivity from the measured electrical resistivity data. Comparing the findings of this study with prior investigations on both pure Fe and Fe-10wt%Ni indicates that an increase in Ni ranging from 0-10wt% has negligible effect on the electrical resistivity of Fe alloys. By comparing the range of estimated heat flux through the core-mantle boundary of 1.5–78 GW to the estimated adiabatic core heat flux ~331 MW at the top of Vesta's core determined in this study, we conclude that the mechanism behind Vesta's past core dynamo that generated its surface magnetic field during its early history was thermal convection.

Keywords

Asteroid 4-Vesta; Electrical resistivity; Magnetic fields; Iron-nickel alloys; High pressure; Experimental techniques; Thermal convection; High temperature.

Summary for Lay Audience

This study explored the inner workings of Vesta, a differentiated planetary body with a metallic core, thought to have emerged during the early formation of our solar system, by conducting high pressure and temperature experiments on a potential core-mimetic alloy. By measuring the electrical resistivity of this alloy under extreme pressure and temperature conditions, we gained insights into Vesta's past magnetic field activity.

The Fe alloy, composed of 95wt% iron and 5wt% nickel (Fe₅Ni), was subjected to temperatures of up to 2000 K, under pressures of 2-5 GPa in a 1000-ton cubic-anvil press, simulating the pressure and temperature conditions deep within Vesta. By measuring its electrical resistivity, its thermal conductivity was calculated, which indicates how efficiently heat travels through the core's outer layer. Using thermal conductivity, the conducted heat flux within Vesta's core was determined.

Applying these findings to Vesta, the second-largest asteroid in our solar system, revealed that during its early history, Vesta likely experienced thermal convection within its core. This means that the liquid core underwent vigorous heat-driven motion. Such movement generates magnetic fields, similar to what we observe on Earth.

The results of this study provide insight on Vesta's past magnetic field and contributes to our understanding of how small celestial bodies can generate magnetic fields through processes like thermal convection.

Co-Authorship Statement

Chapter 3, the body chapter of this thesis, has been published as a peer-reviewed paper in the journal *Crystals*.

My contributions to this chapter included (1) machining the necessary experimental components for the pressure cell, (2) conducting experiments at high pressures and temperatures utilizing a 1000-ton cubic anvil press, (3) analyzing recovered samples after each experimental run with techniques like sample sectioning and microscopy, (4) meticulously analyzing and interpreting the acquired data, and (5) composing and refining the content of the chapter.

Dr. Richard A. Secco's and Dr. Wenjun Yong's contributions to the chapter included: (1) conceptualizing the project, (2) providing financial support for its execution, (3) engaging in discussions centered around the interpretation of the gathered data, and (4) offering constructive feedback on the written manuscript.

Acknowledgments

The completion of this thesis owes a great deal to the invaluable contributions of several individuals. Dr. Wenjun Yong's involvement in experimental runs, Jon Jacobs' expertise in machining experimental components, Steve Woods' efforts in preparing recovered samples, Marc Beauchamp's and Joshua Laughton's contributions to the EMP analysis, and the constant support of Dr. R.A. Secco and his lab team have been indispensable throughout the entire process. The financial support that facilitated this work was generously provided by the Natural Sciences and Engineering Research Council of Canada, grant number RGPIN 2018-05021 to R.A.S., and grant numbers RGPIN-2022-04427 and DGEGR 2022-00151 to W.Y. It is important to note that while these funding agencies played a pivotal role in making this research possible, they were not directly involved in the study's execution.

Table of Contents

Abstract	ii
Summary for Lay Audience	iii
Co-Authorship Statement	iv
Acknowledgments	v
List of Figures	viii
List of Tables	xi
List of Appendices	xii
Chapter 1	1
1 Introduction	1
1.1 Magnetic field generation within planetary bodies	2
1.1.1 Compositional convection vs. thermal convection	3
1.2 Asteroid 4 Vesta	4
1.2.1 History and core composition	5
1.3 Research Objective	6
References	8
Chapter 2	10
2 Methods to probe heat flow in the cores of terrestrial bodies	10
2.1 Significance of studying Fe and Fe alloys	10
2.2 Theoretical (computational) methods	11
2.2.1 Density functional theory	11
2.2.2 Molecular dynamics	13
2.3 Experimental Techniques	13
2.3.1 Static Methods of High P, T Generation	13
2.3.1.1 Diamond anvil cells	14

2.3.1.2 Multi-anvil press.....	14
2.4 Sample Analytical Methods	16
2.5 Current understanding of the electrical resistivity and thermal conductivity Fe and Fe alloys	17
References	20
Chapter 3.....	24
3 Thermal convection in Vesta’s core from experimentally based conductive heat flow estimates	24
3.1 Introduction.....	24
3.2 Methods	25
3.3 Results	28
3.4 Discussion	31
3.5 Conclusions.....	33
References	34
Chapter 4.....	37
4 Conclusion.....	37
4.1 Summary	37
4.2 Suggestions for Future Research.....	38
Appendices.....	40
Appendix A: Additional Cross Sectional Images and EMPA Results	40
A.1 Additional Cross Sectional Images	40
A.2 EMPA Results.....	47
Curriculum Vitae	55

List of Figures

Figure 1.1: Illustration depicting the chronological occurrence of the dynamos of some terrestrial bodies in the inner solar system (Tikoo & Evans, 2022).....	1
Figure 1.2: Schematic diagram of heat flow in a differentiated terrestrial planetary body (Zhang et al., 2022).....	4
Figure 1.3: An image of Asteroid 4 Vesta (NASA/JPL-Caltech/UCLA/MPS/DLR/IDA)	5
Figure 2.1: Graph illustrating the substantial amount of research on experimental and theoretical methods of estimating the ρ of Fe, Fe-Ni, Fe-O and Fe-Si and S alloys at the core conditions of terrestrial planetary bodies (Berrada and Secco, 2021).	10
Figure 2.2: 1000-ton cubic anvil press located at UWO in B&G Building Room 0127.	26
Figure 2.3: Assembled cubic pressure cell (1.25 inches or 3.175 cm edge length) placed on the lower tungsten carbide anvil (1 inch or 2.54 cm edge length) in the 1000-ton cubic anvil press..	27
Figure 2.4: 3D illustrated contour maps showing the recorded resistivity of (A) Fe, (B) Fe-Ni alloys, (C) Fe-O alloys, and (D) Fe-Si/S alloys as a function of P and T (Berrada and Secco, 2021)..	278
Figure 3.1: Schematic diagram of cell design (modified from Ezenwa and Secco, 2017)...	266
Figure 3.2: Cross sectional image of Fe-5 wt% Ni recovered from 4 GPa and 1986 K (a) Cross sectional image of a polishing stage of the sample (b) Cross sectional image of a polishing stage of the sample with the value for the length and diameter recorded.	277
Figure 3.3: Chemical composition of Fe-5 wt% Ni recovered from three separate experiments at 4 GPa that reached maximum T of: (a) 1738 K ($T_{\text{melt}} - 55$ K); (b) 1847 K ($T_{\text{melt}} + 54$ K); and (c) 1986 K ($T_{\text{melt}} + 193$ K).	299
Figure 3.4: Comparison of the electrical resistivity of Fe-5 wt% Ni and Fe-10 wt% Ni (Silber et al., 2018; Ho et al., 1983; Lenhart and Secco, 2022; Pommier, 2020; Yin et al., 2022). 3030	

Figure 3.5: Comparison of thermal conductivity of Fe-5 wt% Ni and Fe-10 wt% Ni (Ho et al.,1983; Lenhart and Secco, 2022; Pommier, 2020).....	30
Figure 3.6: High pressure electrical resistivity and thermal conductivity data at 1800 K from this study plotted with 1 atm data (Ho et al.,1983) for purpose of interpolation to Vestan CMB pressure of 0.2 GPa.	311
Figure A.1.1: Cross sectional image of the initial polishing stage of Fe-5 wt% Ni recovered from 2 GPa and 1896 K.	40
Figure A.1.2: Cross sectional image of the middle polishing stage of Fe-5 wt% Ni recovered from 2 GPa and 1896 K.	Error! Bookmark not defined.
Figure A.1.3: Cross sectional image of the end polishing stage of Fe-5 wt% Ni recovered from 2 GPa and 1896 K.	41
Figure A.1.4: Cross sectional image of the initial polishing stage of Fe-5 wt% Ni recovered from 3 GPa and 1960 K.	42 Error! Bookmark not defined.
Figure A.1.5: Cross sectional image of the middle polishing stage of Fe-5 wt% Ni recovered from 3 GPa and 1960 K.	Error! Bookmark not defined. 2
Figure A.1.6: Cross sectional image of the end polishing stage of Fe-5 wt% Ni recovered from 3 GPa and 1960 K.	43
Figure A.1.7: Cross sectional image of the initial polishing stage of Fe-5 wt% Ni recovered from 4 GPa and 1982 K.	43
Figure A.1.8: Cross sectional image of the middle polishing stage of Fe-5 wt% Ni recovered from 4 GPa and 1982 K.	44
Figure A.1.9: Cross sectional image of the end polishing stage of Fe-5 wt% Ni recovered from 4 GPa and 1982 K.	44
Figure A.1.10: Cross sectional image of the initial polishing stage of Fe-5 wt% Ni recovered from 5 GPa and 2077 K.	45

Figure A.1.11: Cross sectional image of the middle polishing stage of Fe-5 wt% Ni recovered from 5 GPa and 2077 K.	45
Figure A.1.12: Cross sectional image of the end polishing stage of Fe-5 wt% Ni recovered from 5 GPa and 2077 K.	46
Figure A.2.1: Annotated diagram of the locations of target spots on the sample recovered from 4 GPa and 1982 K.	47
Figure A.2.2: Annotated diagram of the locations of target spots on the sample recovered from 5 GPa and 2077 K.	49
Figure A.2.3: Annotated diagram of the locations of target spots on the sample recovered from 4 GPa and 1723 K.	51
Figure A.2.4: Annotated diagram of the locations of target spots on the sample recovered from 4 GPa and 1847 K.	53

List of Tables

Table 2.1: Overview of the electrical resistivity and thermal conductivity of the Earth's core from some recent studies in this past decade (Yin et al., 2022).....	17
Table A.2.1: Summary of the mineral composition of each target spot on the sample recovered at 4 GPa and 1982 K	48
Table A.2.2: Summary of the mineral composition of each target spot on the sample recovered at 5 GPa and 2077 K	50
Table A.2.3: Summary of the mineral composition of each target spot on the sample recovered at 4 GPa and 1723 K	52
Table A.2.4: Summary of the mineral composition of each target spot on the sample recovered at 4 GPa and 1847 K	54

List of Appendices

Appendix A: Additional Cross Sectional Images and EMPA Results.	40
--	----

Chapter 1

1 Introduction

The magnetic field of a planetary body protects the surface of that body from the charged particles and cosmic radiation emitted by the Sun and has become one important indicator of the potential of a planet to sustain life. Most terrestrial bodies have or have had a magnetic field. The chronological occurrence of the dynamos attributed to the generation of magnetic fields in terrestrial planetary bodies can be inferred from paleomagnetism, remanent crustal magnetism, and also the detection of active dynamo fields by spacecraft. Figure 1.1 illustrates the chronological occurrence of the dynamos of some terrestrial bodies in the inner solar system, with the time periods characterized by black bars and shaded intervals indicating dynamo activity, and the question marks representing time periods with insufficient data to determine the presence or absence of a dynamo (Tikoo & Evans, 2022).

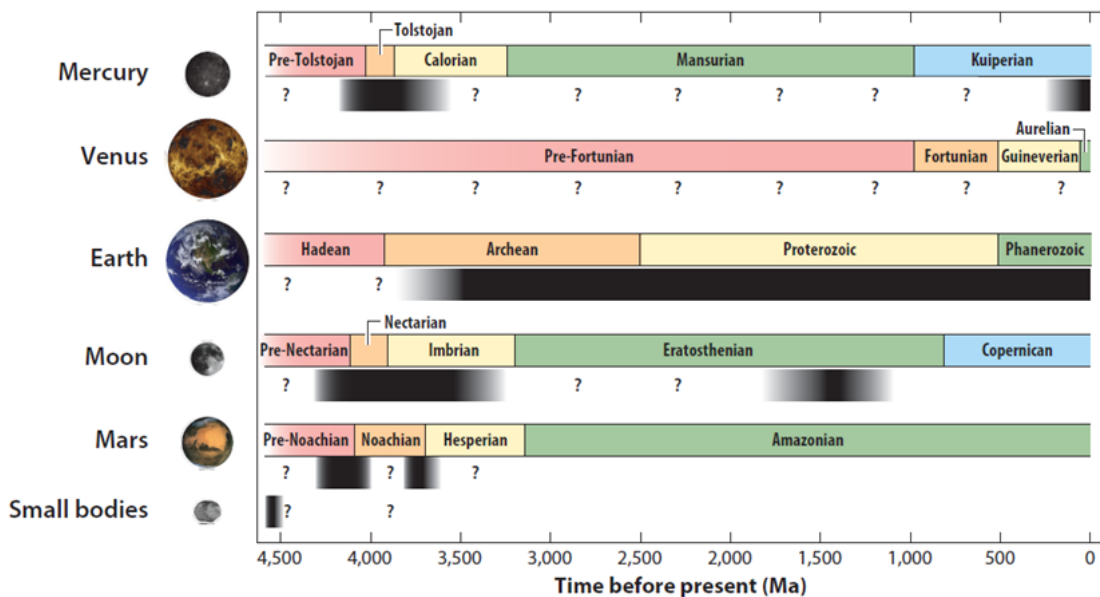


Figure 1.1: Illustration depicting the chronological occurrence of the dynamos of some terrestrial bodies in the inner solar system (Tikoo & Evans, 2022).

For terrestrial bodies like Earth, Mars, Mercury, the Moon, Ganymede and Vesta, their possession of magnetic fields (present or past) is explained by the physical properties,

chemical behaviors and phase diagrams of the metallic alloys in their cores. The physical properties of these alloys provide valuable data used in modelling the thermal and magnetic evolution of terrestrial bodies. Physical properties of alloys at core pressure (P) and temperature (T) conditions may be determined by experimental techniques conducted at high P, T because the depths to the cores of these bodies make them inaccessible to direct observation even with present day technology. The general purpose of this research is to use experimental methods to gain information about the conductive heat flow at the top of the core of a terrestrial body, Asteroid 4 Vesta, in order to deduce if thermal convection could have been the source of a magnetic field in a body that no longer possesses one.

1.1 Magnetic field generation within planetary bodies

From considerations of the law of conservation of energy, the thermal energy of a planetary core may be converted to kinetic energy by thermal convection which is then converted to electromagnetic energy by the dynamo effect. The magnetic fields of most terrestrial bodies are produced by a dynamo generated by the convection and rotation of the electrically conductive fluid contained in the outer core (Buffett, 2000). Planetary bodies like Mars and Vesta do not currently possess a magnetic field but paleomagnetic studies of meteorites from these bodies indicate that they once possessed a magnetic field (Stevenson, 2001; Fu et al., 2012).

From our understanding of the best studied magnetic field, Earth's geomagnetic field, if there is no continuous driving force for fluid motion, the processes responsible for generating the magnetic field in the core will eventually dissipate. All core materials possess electrical resistance, which results in the dissipation of energy in the form of heat, known as Ohmic dissipation. The minimum energy required to sustain the dynamo can be estimated by measuring the amount of Ohmic heating (Jones, 2007). The Earth's geomagnetic field has been detected in rock formations dating as far back as 3.5 billion years (Tarduno et al., 2010) indicating that the field has existed for a long time. Therefore, it is evident that a continuous source (or sources) of energy has (have) been available to generate the geomagnetic field.

The two possible mechanisms that could have generated past core dynamo in planetary bodies that no longer possess a magnetic field are compositional convection, as explained below, and/or thermal convection. Paleomagnetic records also reveal the past strength and direction of a magnetic field, but understanding heat flow in the core provides insight into how the field was generated at various stages of the planetary body's history. For example, even though the Earth's geomagnetic field is known to have operated for much of its existence, it is still not clear if the dynamo has always been driven by thermal convection, compositional convection, or a combination of both, perhaps with varying contributions of each over time.

1.1.1 Compositional convection vs. thermal convection

The process of compositional (also called chemical) convection is caused by the freezing of the outer core alloy of Fe-Ni + X (where X may be S, Si, O etc), resulting in the settling of pure Fe onto the solid inner core, creating a higher concentration of lighter elements (S, Si, O, etc) in the liquid above the inner core boundary (ICB). The lowering of the density at this boundary as a result of the freezing out of pure Fe causes a churning motion in the liquid, driven by buoyancy. The less dense and light element-enriched liquid above the ICB rises outward and displaces the denser and more Fe rich liquid above. The way the Earth's solid inner core was formed and continues to grow is likely the main driving force behind the geodynamo today (Braginsky, 1963; Loper, 1978).

From the study by Zhang et al. (2022), the uppermost outer core exhibits thermal stratification since the adiabatic heat flux in the core, Q_a , is greater than the heat flux across the core-mantle boundary (CMB), Q_{cmb} . This stratified layer prevents thermally generated radial convection and so it is inferred that the geodynamo is primarily driven by compositional convection beneath the stratified layer, as illustrated in Fig. 1.2. This compositional convection is linked to the partitioning of light elements during the crystallization of the inner core.

Thermal convection within a planetary body typically decreases since the thermal gradient is reduced as the body loses internal heat over time. The thickness and composition of the mantle also play key roles in the generation of a dynamo in the core,

as a thinner and lower thermal conductivity silicate mantle make it less likely for a dynamo to form (Freitas et al., 2021). This is because the mantle controls the heat flow out of the core (Olson, 2016), dictating the need for thermal convection in the outer core. If the conducted heat flow, which is determined by the thermal conductivity of the core material, delivered through the core to and across the CMB satisfies the draw of heat by the mantle, then thermal convection is not needed in the core. Therefore, the amount of heat drawn from the outer core by the mantle, along with the conductive heat flow within the core, determines the presence/absence of thermal convection.

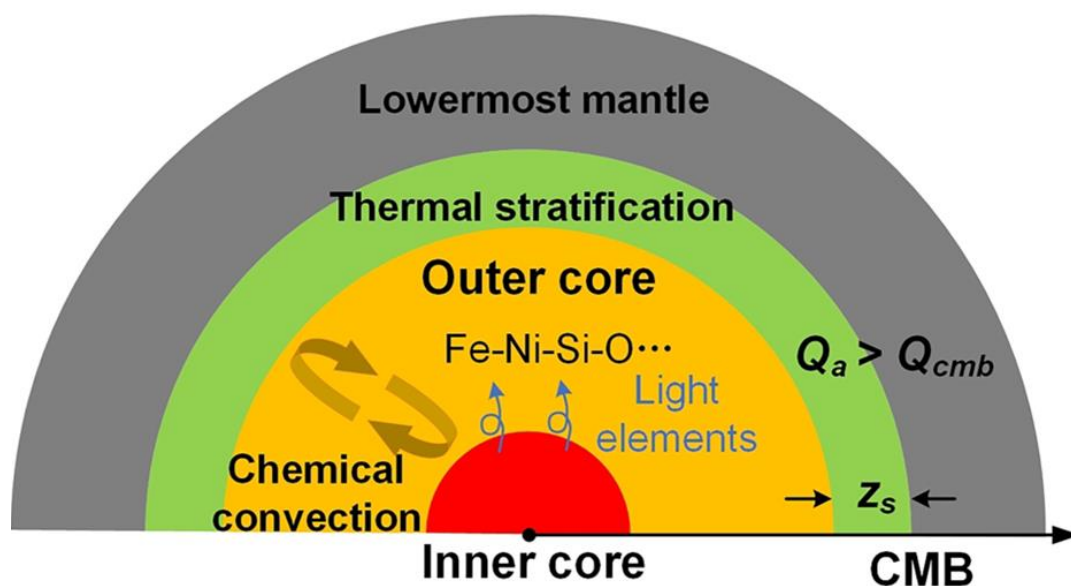


Figure 1.2: Schematic diagram of heat flow in a differentiated terrestrial planetary body showing the adiabatic heat flow (Q_a) exiting the core and the thickness of thermal stratification (Z_s) at the top of the outer core in relation to the Core-Mantle Boundary (CMB) heat flow (Q_{cmb}) (Zhang et al., 2022).

1.2 Asteroid 4 Vesta

According to Chambers (2004), terrestrial planets were created through the gradual accumulation and merging of protoplanetary objects that were less than 1000 km in diameter. Some of these protoplanets are still in existence today, including Asteroid 4 Vesta (Fig. 1.3), which is the second most massive asteroid and the source of howardite-eucrite-diogenite (HED) meteorites. Vesta's landscape is filled with craters (Fig. 1.3),

providing evidence of numerous meteoroid and asteroid impacts that occurred during the early stages of the solar system. Vesta is a differentiated body that has an inner core, and its high density, original basaltic crust, and substantial size suggest that it is a complete remnant of the early solar system that avoided being disrupted by catastrophic collisions (Russell et al., 2012). The overall surface color variations observed by Reddy et al (2012), corroborates Vesta's differentiation and the analysis of the data gathered by the visual and infrared spectrometers on the Dawn spacecraft indicates that it had a complex magmatic evolution resulting in its differentiated crust and mantle (De Sanctis et al., 2012).

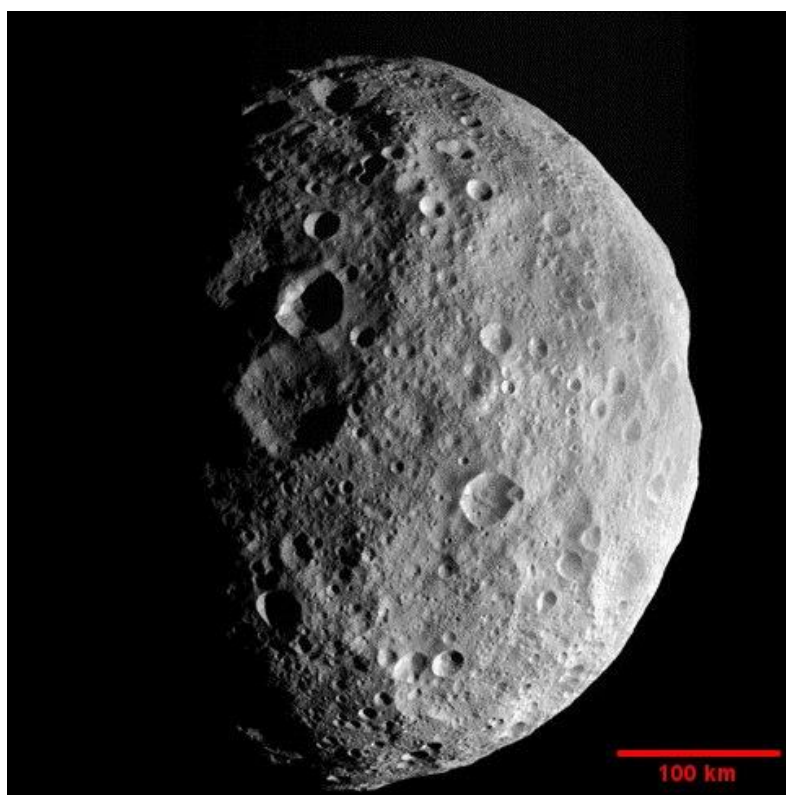


Figure 1.3: An image of Asteroid 4 Vesta (NASA/JPL-Caltech/UCLA/MPS/DLR/IDA)

1.2.1 History and core composition

Vesta's core composition is assumed to be similar to that of the liquid outer cores of terrestrial planetary bodies, which are primarily composed of Fe and Ni (Poirier, 1994),

with smaller amounts of lighter elements such as Si, O, S, H, C, and Mg. Samples from Vesta's interior are unavailable, so meteorite samples assumed to originate from Vesta are used as a proxy in understanding the cooling rates of its interior (Weiss et al., 2010). These samples provide estimates of heat flow out of the core and into the mantle.

Paleomagnetic research has shown that Vesta once had an internally generated magnetic field, as evidenced by the natural remnant magnetization of the Eucrite ALHA81001 meteorite (Fu et al., 2012), which suggests that Vesta possessed a liquid metallic core. The inference of an early dynamo on Vesta from paleomagnetic studies provides further support for the theory that dynamos could have formed in small differentiated protoplanetary objects during the early stages of the solar system (Stevenson, 2010). The existence of a magnetized crust indicates that some parts of Vesta's surface had already solidified and cooled below the Curie temperature when the dynamo was active and the high intensity of the remaining crustal magnetization suggests that the dynamo likely generated surface fields with intensities ranging from 10 to 100 μT (Fu et al., 2012).

Vesta is not in hydrostatic equilibrium, as evidenced by the presence of basins (Russell et al., 2012) on its surface, disqualifying it from being classified as a dwarf planet. However, the fact that Vesta has a differentiated core makes it relevant for this research. The use of Fe-Ni alloy for this research is informed by the results of numerous studies done on meteorites assumed to originate from Vesta which possess at least 4wt% nickel (Fu et al., 2012).

1.3 Research Objective

The goal of this study is to determine if thermal convection played a role in the past magnetic field generation on the asteroid Vesta. To do this, electrical resistivity of a liquid Fe alloy composed of 95wt% Fe and 5wt% Ni (Fe5Ni) was measured at elevated T up to 2000 K and P of 2-5 GPa in a 1000-ton cubic-anvil press. These measurements were used to calculate the thermal conductivity of Fe5Ni and estimate the conductive heat flow at the top of Vesta's core.

By comparing the estimated conductive heat flow at the top of Vesta's core to existing estimates of heat flow through its early CMB, it is possible to infer whether thermal convection occurred in Vesta's core. As Vesta does not currently have an internally generated magnetic field, this research is particularly relevant for understanding Vesta's earliest history, based on evidence of an internally generated magnetic field from meteorite records when heat flow was higher (Fu et al., 2012). In addition, the results of this research also provide general insight into how terrestrial bodies generate magnetic fields particularly with respect to the balance between conducted and convected heat flow in their cores.

References

- Braginsky, S.I. 1963. Structure of the F layer and reasons for convection in Earth's core. Dokl. Akad. Nauk. SSSR English Translation. 149: 1311-1314.
- Buffett, B. A., (2000) Earth's core and the geodynamo. *Science* 288: 2007–2012.
- Chambers, J. E. (2004). Planetary accretion in the inner Solar System. *Earth and Planetary Science Letters*, 223(3–4), 241–252.
<https://doi.org/10.1016/j.epsl.2004.04.031>.
- De Sanctis, M. C., Ammannito, E., Capria, M. T., Tosi, F., Capaccioni, F., Zambon, F., Carraro, F., Fonte, S., Frigeri, A., Jaumann, R., Magni, G., Marchi, S., McCord, T. B., McFadden, L. A., McSween, H. Y., Mittlefehldt, D. W., Nathues, A., Palomba, E., Pieters, C. M., ... Turrini, D. (2012). Spectroscopic Characterization of Mineralogy and Its Diversity Across Vesta. *Science*, 336(6082), 697–700.
<https://doi.org/10.1126/science.1219270>.
- Freitas, D., Monteux, J., Andrault, D., Manthilake, G., Mathieu, A., Schiavi, F., & Cluzel, N. (2021). Thermal conductivities of solid and molten silicates: Implications for dynamos in mercury-like proto-planets. *Physics of the Earth and Planetary Interiors*, 312, 106655. <https://doi.org/10.1016/j.pepi.2021.106655>.
- Fu, R. R., Weiss, B. P., Shuster, D. L., Gattacceca, J., Grove, T. L., Suavet, C., Lima, E. A., Li, L., & Kuan, A. T. (2012). An Ancient Core Dynamo in Asteroid Vesta. *Science*, 338(6104), 238–241. <https://doi.org/10.1126/science.1225648>.
- Jones, C. (2007). Thermal and Compositional Convection in the Outer Core. In *Volume 8: Core Dynamics* (Vol. 8, pp. 131–185). Elsevier. <https://doi.org/10.1016/B978-044452748-6/00130-9>.
- Loper, D. E. (1978). The gravitationally powered dynamo. *Geophysical Journal International*, 54(2), 389–404. <https://doi.org/10.1111/j.1365-246X.1978.tb04265.x>.
- Olson, P. (2016). Mantle control of the geodynamo: Consequences of top-down regulation. *Geochemistry, Geophysics, Geosystems*, 17(5), 1935–1956.
<https://doi.org/10.1002/2016GC006334>.
- Poirier, J. P., (1994) Light elements in the Earth's outer core: A critical review. *Physics of the Earth and Planetary Interiors*, 85(3), 319–337.
[https://doi.org/https://doi.org/10.1016/0031-9201\(94\)90120-1](https://doi.org/https://doi.org/10.1016/0031-9201(94)90120-1).
- Reddy, V., Nathues, A., Le Corre, L., Sierks, H., Li, J.-Y., Gaskell, R., McCoy, T., Beck, A. W., Schröder, S. E., Pieters, C. M., Becker, K. J., Buratti, B. J., Denevi, B., Blewett, D. T., Christensen, U., Gaffey, M. J., Gutierrez-Marques, P., Hicks, M.,

- Keller, H. U., ... Russell, C. (2012). Color and Albedo Heterogeneity of Vesta from Dawn. *Science*, 336(6082), 700–704. <https://doi.org/10.1126/science.1219088>.
- Russell, C. T., Raymond, C. A., Coradini, A., McSween, H. Y., Zuber, M. T., Nathues, A., De Sanctis, M. C., Jaumann, R., Konopliv, A. S., Preusker, F., Asmar, S. W., Park, R. S., Gaskell, R., Keller, H. U., Mottola, S., Roatsch, T., Scully, J. E. C., Smith, D. E., Tricarico, P., ... Titus, T. N. (2012). Dawn at Vesta: Testing the Protoplanetary Paradigm. *Science*, 336(6082), 684–686. <https://doi.org/10.1126/science.1219381>.
- Stevenson, D. J. (2001). Mars' core and magnetism. *Nature*, 412(6843), 214–219. <https://doi.org/10.1038/35084155>.
- Stevenson, D. J. (2010). Planetary Magnetic Fields: Achievements and Prospects. *Space Science Reviews*, 152(1–4), 651–664. <https://doi.org/10.1007/s11214-009-9572-z>.
- Tikoo, S. M., & Evans, A. J. (2022). Dynamos in the Inner Solar System. *Annual Review of Earth and Planetary Sciences*, 50(1), 99–122. <https://doi.org/10.1146/annurev-earth-032320-102418>.
- Tarduno, J. A., Cottrell, R. D., Watkeys, M. K., Hofmann, A., Doubrovine, P. V., Mamajek, E. E., Liu, D., Sibeck, D. G., Neukirch, L. P., & Usui, Y. (2010). Geodynamo, Solar Wind, and Magnetopause 3.4 to 3.45 billion Years Ago. *Science*, 327(5970), 1238–1240. <https://doi.org/10.1126/science.1183445>.
- Weiss, B. P., Gattacceca, J., Stanley, S., Rochette, P., & Christensen, U. R. (2010). Paleomagnetic Records of Meteorites and Early Planetary Differentiation. *Space Science Reviews*, 152(1–4), 341–390. <https://doi.org/10.1007/s11214-009-9580-z>.
- Zhang, Y., Luo, K., Hou, M., Driscoll, P., Salke, N. P., Minár, J., Prakapenka, V. B., Greenberg, E., Hemley, R. J., Cohen, R. E., & Lin, J.-F. (2022). Thermal conductivity of Fe-Si alloys and thermal stratification in Earth's core. *Proceedings of the National Academy of Sciences*, 119(1), e2119001119. <https://doi.org/10.1073/pnas.2119001119>.

Chapter 2

2 Methods to probe heat flow in the cores of terrestrial bodies

2.1 Significance of studying Fe and Fe alloys

The composition of the Earth's core is thought to consist primarily of iron, nickel, and a small proportion of light elements such as silicon, sulfur, oxygen, carbon, nitrogen, and hydrogen, as well as phosphorus (Poirier, 1994). The thermal conductivities of these constituent elements play a significant role in determining the adiabatic heat flow within the Earth's core and the metallic cores of other terrestrial bodies, which is inextricably connected to the generation of a dynamo within those bodies.

Although a significant body of research exists on the electrical resistivity and thermal conductivity of Fe under conditions of planetary interiors, there are relatively fewer studies that have investigated Fe alloys under different planetary core conditions. In the past two decades, a substantial amount of work has been conducted in this field to expand our collective understanding of the core properties and heat flow of terrestrial planetary bodies as shown in Figure 2.1.

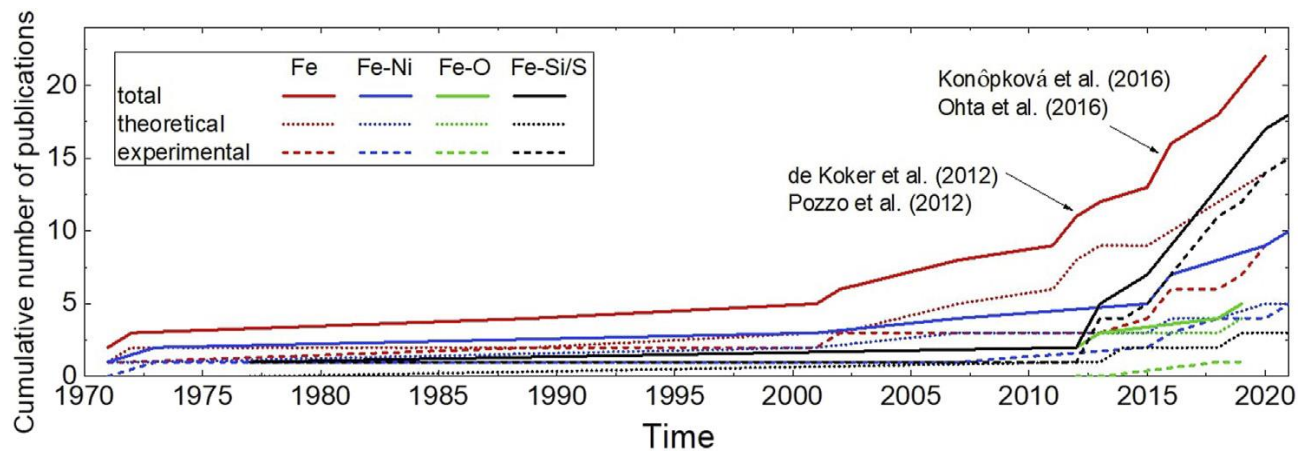


Figure 2.1: Graph illustrating the substantial amount of research on experimental and theoretical methods of estimating the ρ of Fe, Fe-Ni, Fe-O and Fe-Si and S alloys at the core conditions of terrestrial planetary bodies (Berrada and Secco, 2021).

A combination of experimental and theoretical investigations has been used in expanding our understanding of heat flow in metal alloys within the cores of terrestrial planets (Berrada and Secco, 2021). In order to gain insights into planetary core thermal properties, including the scope of this study, methods involving high P, T experimentation on Fe alloys are being employed. Also, theoretical approaches, utilizing molecular level models such as density functional theory and molecular dynamics, are essential in complementing experimental findings by enhancing our understanding of thermal properties of Fe alloys as they directly relate to thermal processes in the core.

2.2 Theoretical (computational) methods

Computational methods provide a means to calculate the electronic and atomic structure as well as, elastic properties of Fe and Fe alloy systems within terrestrial planetary bodies. These methods can be broadly classified into two categories: computations of atomic or molecular motion and computations of the electronic structure for a given composition (Alfè, 2015).

2.2.1 Density functional theory

Density functional theory (DFT) is a method used to investigate the elasticity and phase stability of compressed materials in their ground electronic state. To calculate the exchange and correlation between electrons in energy computations, other approximations such as generalized gradient approximation (GGA) and local density approximation (LDA) are employed in conjunction with DFT (Duffy et al., 2015). While DFT methods have been extensively tested for various planetary materials, their performance under extreme conditions of giant planets and exoplanets remains less validated since DFT relies on pseudopotentials that exclude core electrons. The reason is that in such large planetary bodies where very high pressures exist, core electrons may participate in exchange and correlations with other electrons. Methods that employ LDA and GGA exhibit approximately 15% accuracy for elastic constants, approximately 5% for vibrational frequencies, and approximately 1-2% for bond lengths and unit cell dimensions (Oganov et al., 2013).

Ab initio simulations that consider both thermal disorder and electronic correlations have also been used to study the thermal conductivity and electrical resistivity of Fe under the extreme conditions in the Earth's inner core. The results from Pourovskii et al. (2020) demonstrate the importance of considering thermal disorder and electronic correlations in *ab initio* simulations to accurately understand the transport properties of Fe under extreme conditions, and their main findings hold true for both of the most likely Fe phases in Earth's inner core. The knowledge gained from these simulations can be valuable input for geophysical models of the Earth's core. The study reveals that thermal disorder reduces the non-Fermi-liquid behavior of the body-centered cubic Fe phase, leading to a decrease in electron-electron scattering (EES) in Fe. This EES in Fe has no significant effect on its thermal conductivity and electrical resistivity at the Earth's core conditions. Furthermore, the study reveals that EES also remains weak in the hexagonal close-packed Fe phase even under the influence of thermal disorder and that the breaking of Matthiessen's rule observed with increasing EES occurs as a result of the interplay between EES and electron-lattice scattering (Pourovskii et al., 2020).

Recent *ab initio* simulations like the spin-polarized DFT simulation reduce the discrepancies between experimental and spin-degenerate simulation results for electrical resistivities and thermal conductivities from more than 30% to within 10%. The study by Korell et al. (2019) uses the Kubo-Greenwood formalism to calculate the thermal conductivity and electrical resistivity of liquid Fe over a significant range of pressure and temperature. This study reveals that a stable paramagnetic state persists in the liquid at high temperatures and ambient pressure, and it explores the persistence of magnetic fluctuations at elevated densities along the 3700 K isotherm. As the pressure exceeds 20-50 GPa, the liquid transforms into a diamagnetic state, indicating a continuous transition from paramagnetic to diamagnetic behavior. Such a transition has a notable impact on the physical properties of liquid Fe, particularly its electrical resistivities and thermal conductivities, and it could hold significance for dynamo processes in Mercury and Mars (Korell et al., 2019).

2.2.2 Molecular dynamics

Molecular dynamics (MD) or Monte Carlo (MC) techniques were among the initial computational models developed for this field. They involve using appropriate inter-atomic potentials to apply equations of motion in order to monitor the thermal motion of nuclei (hence ignoring electronic interactions) to extract dynamical properties at high temperatures and/or pressures. By applying Newton's equations of motion (e.g., $F_i = m_i * dv_i/dt$), which account for forces (F), change of velocities (v) with time (t), and masses of atoms (m), MD simulations enable us to understand planetary and exoplanetary evolution, by modelling changes in transport properties, electrical behavior, viscosities, and diffusion (Swift et al., 2011) induced by T and P. Path integral MD is a highly precise quantum simulation method that considers both nuclei and electrons and encompasses all correlation effects. MD methods provide a comprehensive description of matter, even up to fully ionized plasma states, and are highly efficient computational methods even for temperatures up to 5000 K. For lower temperatures, it is more computationally efficient to employ a ground state simulation method such as quantum MD, as path integral MD calculations become computationally expensive (Ceperley, 2010).

2.3 Experimental Techniques

Experimental techniques for investigating the physical properties, crystal structures, melting boundaries, phase diagrams, and chemical behavior of Fe and Fe alloys at high temperature and pressure have been developed since the 1900s. P. W. Bridgman is widely regarded as the pioneer of modern high pressure physics (Nellis, 2010). Bridgman's contributions have laid the foundation for advancements in understanding materials at the core pressure and temperature conditions of terrestrial planetary bodies.

2.3.1 Static Methods of High P, T Generation

Static high pressure devices exert concentrated force on a small area, allowing for the generation of static high P. This method provides sufficient time for thermodynamic equilibrium to be achieved at constant P, T conditions, as measurements are conducted

under hydrostatic or quasi-hydrostatic conditions. In static high P experiments, the sample volume decreases as the P increases.

2.3.1.1 Diamond anvil cells

The diamond anvil cell (DAC) is a widely used device for generating high pressures and temperatures and is known for its effectiveness and cost-efficiency. DACs are often called small volume presses due to their use of smaller sample volumes to achieve higher pressures. The laser-heated DAC has been used to successfully replicate the extreme temperature and pressure conditions found in the Earth's inner core (Tateno et al., 2010). In a DAC, a thin metal foil gasket with a small hole (on the order of 100 μm in diameter) forms the pressure chamber housing the sample. Two opposing diamonds compress the gasket and pressure chamber converting the applied force into hydrostatic pressure using a gas pressure-transmitting medium and a quasi-hydrostatic pressure using a solid pressure-transmitting medium.

DACs use laser radiation from a CO_2 or Nd:YAG (yttrium–aluminum–garnet) laser to heat the sample because the transparent diamond anvils allow it to effectively transmit laser radiation to be absorbed by the sample for heating purposes. Technological advancements, such as the double-sided laser heating system, have improved temperature stability, maximum temperature limits, and reduced temperature gradients.

2.3.1.2 Multi-anvil press

The multi-anvil press (MAP) uses a hydraulic system that applies force to bring the anvils together. An example of a MAP is the 1000-ton cubic anvil press at Western University shown in Figure 2.2. MAPs yield experimental results that are associated with a lower and narrower range of P and T because they utilize a larger sample volume and provide more homogeneous P and T fields and stable T conditions compared to DAC. This advantage makes MAP's particularly well-suited for precisely determining the phase relations and high T physical properties of minerals in the Earth's mantle (Ishii et al., 2019), but also for synthesizing novel materials at high P (Ovsyannikov et al., 2016). For smaller planetary bodies such as the Moon, Mercury, Mars, Ganymede, and asteroids such as 4 Vesta, MAP's can simulate P, T conditions in the core region.

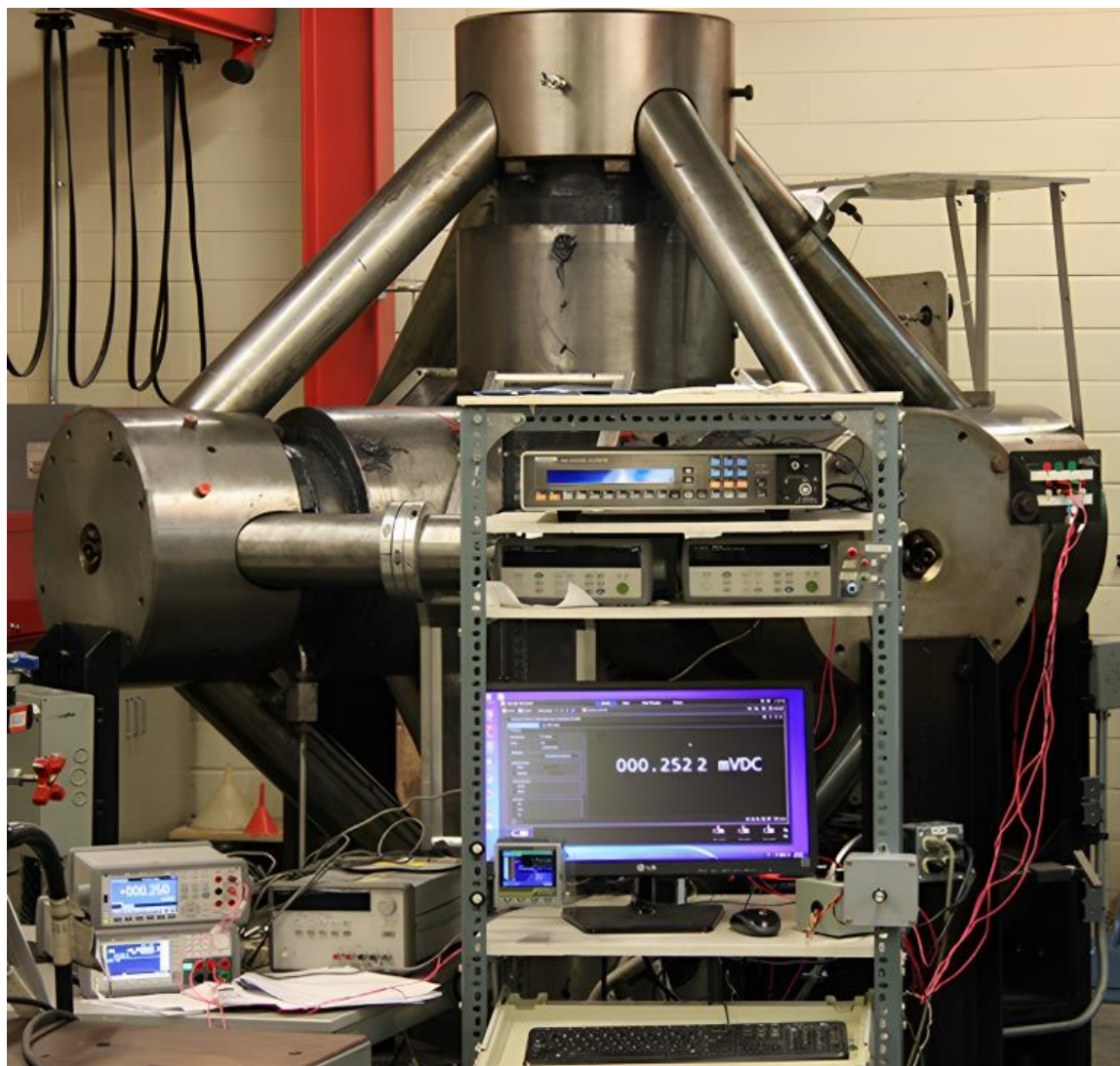


Figure 2.2: 1000-ton cubic anvil press located at UWO in B&G Building Room 0127.

MAPs can achieve P of over 20 GPa using tungsten carbide cubes and up to 100 GPa with sintered diamond cubes (Zhai and Ito, 2011). Figure 2.3 shows the assembled cubic pressure cell with a 1.25 inch edge length positioned within the 1000-ton cubic anvil press. MAP's use resistive heating methods incorporated into the assembled cell design, utilizing materials such as graphite, LaCrO_3 , or rhenium foil, to generate high T . However, a drawback of this heating method is that it cannot maintain stable heating above 2000 K for extended durations, typically limited to a few hours (Zhang and Fei, 2008).



Figure 2.3: Assembled cubic pressure cell (1.25 inches or 3.175 cm edge length) placed on the lower tungsten carbide anvil (1 inch or 2.54 cm edge length) in the 1000-ton cubic anvil press.

2.4 Sample Analytical Methods

The field of high P and T mineral physics has seen advancements in analytical methods, because of the improvement of spatial sensitivity and resolution in various techniques. These technological developments have enhanced studies related to element partitioning, equation of state, transport properties, as well as the detection of melting points, chemical reactions, and phase transitions in compressed samples.

Ex-situ analysis of compressed samples is made possible by performing quenching, decompression, and sample recovery. Various analytical tools such as X-ray diffractometers, electron microprobes, Raman spectrometers, mass spectrometers, and optical microscopes can be utilized for *ex-situ* analysis. The advancement of sample

preparation techniques such as focused ion beam and ion slicers, as well as the availability of nano-analytical instruments such as nanoscale secondary ion mass spectrometer and transmission electron microscopes, have facilitated the application of *ex-situ* analytical methods. These methods enable the study of recovered compressed samples from high pressure and temperature experiments conducted in a MAP (Sakai et al., 2006; Li and Fei, 2014). High-resolution x-ray tomography and radiography are additional *in-situ* analytical methods used to visualize the internal geometry of components within an opaque sample, particularly in MAP experiments conducted at synchrotron facilities (Terasaki et al., 2011).

2.5 Current understanding of the electrical resistivity and thermal conductivity Fe and Fe alloys

Using many of the techniques described above, recent research has extensively examined the electrical resistivity (ρ) and thermal conductivity (κ) of Fe and Fe alloys under the extreme pressure and temperature conditions of the core of various planetary bodies such as the Earth, Mars, Mercury, the Moon, and Ganymede. Table 2.1 presents an overview of the electrical resistivity and thermal conductivity of the Earth's core from some recent studies.

Table 2.1: Overview of the electrical resistivity and thermal conductivity of the Earth's core from some recent studies in this past decade (Yin et al., 2022).

Core materials	ρ_{CMB} ($\mu\Omega \text{ cm}$)	κ_{CMB} (Wm ⁻¹ K ⁻¹)	Method	References
Hcp-Fe (S ^a)	~ 40.4	~ 226	ERM	Ohta et al. (2016)
Hcp-Fe (S ^a)	$\sim 80 \pm 5$	100 ± 10	ERM	Zhang et al. (2020)
Hcp-Fe (L)	195 ± 60	$\sim 42 \pm 12$	ERM	Basu et al. (2020)
Fe-9Si (wt%) (L)	178 ± 1	$\sim 41 - 60$	ERM	Seagle et al. (2013)
Fe-hcp (S ^a)	-	97	FPC	Xu et al. (2018)
Fe-Si-O (L)	~ 110	100	FPC	Pozzo et al. (2013)
Fe (bcc/hcp) (S ^a)	-	-	FPC	Pourovskii et al. (2020)
Fe-Ni (L)	~ 87	125 ± 9	FPC	Li et al. (2021)
Fe-Ni-(C, O, Si, S ^b)		-	FPC	Zidane et al. (2020)
Fe-(Si, S ^b , O)	$\sim 63 - 100$	-	FPC	Wagle et al. (2019)
Fe-hcp (L)	-	25 ± 7	DTCM	Konôpková et al. (2016)
Fe-hcp (L)	-	40 ± 16	DTCM	Saha et al. (2020)
Fe-15Si (at%) (L)	-	~ 20	DTCM	Hsieh et al. (2020)

Notes: S^a, solid state; L, liquid state; C, carbon; O, oxygen; Si, silicon; S^b, sulfur; ERM, electrical resistivity measurements; FPC, first principles calculation; DTCM, direct thermal conductivity measurements.

The low electrical resistivity and high thermal conductivity of pure Fe is inadequate to sustain an early geodynamo driven by thermal convection. To meet the necessary conditions for a thermal convection driven geodynamo in the early stages of Earth's development, it is essential for suitable light elements to be incorporated in the Earth's core, effectively increasing the electrical resistivity and decreasing the thermal conductivity of Fe. This explains the reason for the many investigations of Fe alloy systems in relation to the core of terrestrial planetary bodies that appear in recent reviews (Berrada and Secco, 2021; Yin et al., 2022).

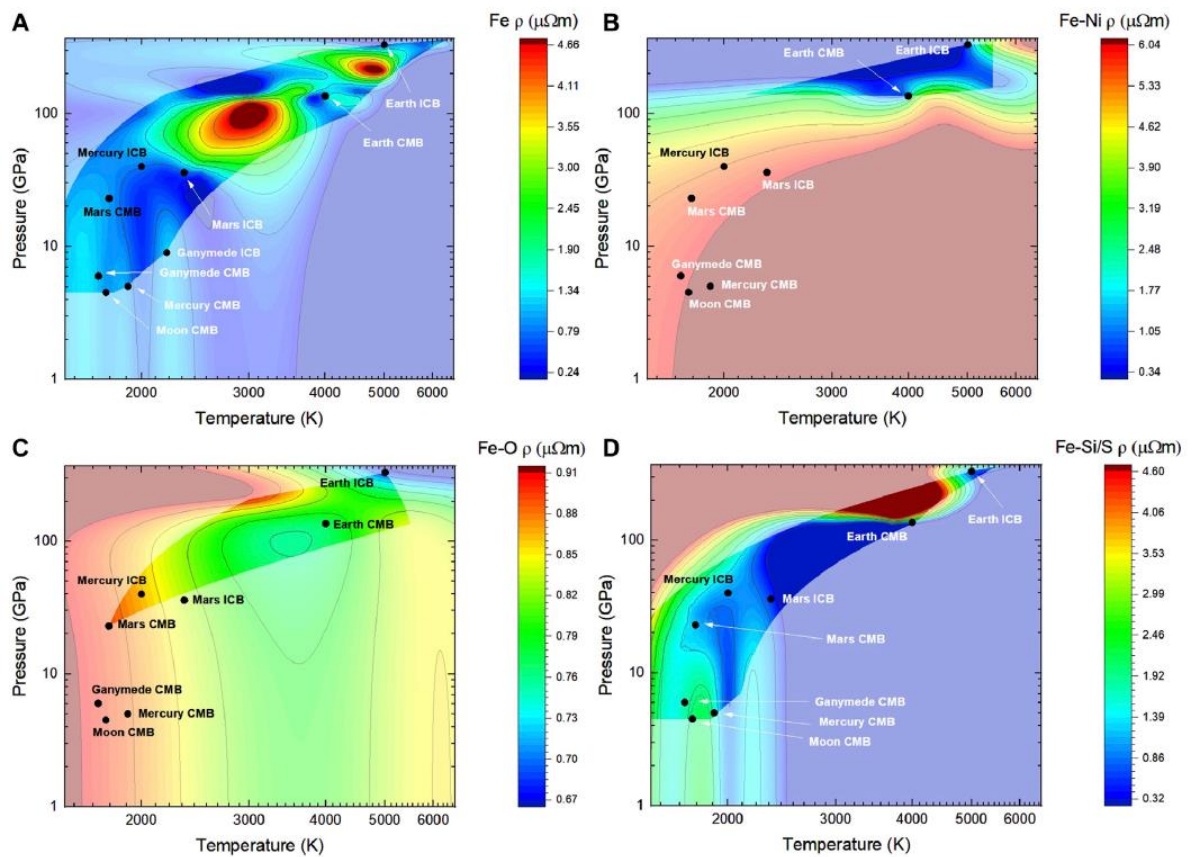


Figure 2.4: 3D illustrated contour maps showing the recorded resistivity of (A) Fe, (B) Fe-Ni alloys, (C) Fe-O alloys, and (D) Fe-Si/S alloys as a function of P and T (Berrada and Secco, 2021).

Contour maps of electrical resistivity values which encompass a wide range of P and T conditions relevant to planetary core conditions have been generated using the existing literature data for the resistivity of various compositions, such as Fe, Fe-Ni alloys, Fe-O alloys, and Fe-Si/S alloys and are shown in Figure 2.4. These maps highlight the unique patterns visible when resistivity is plotted against P and T for each composition. The contour map specifically for Fe-Si/S alloys aligns well with the reported data for planetary core conditions on the Earth, the Moon, Mercury, Mars, and Ganymede (Berrada and Secco, 2021).

Additional research focusing on the investigation of Fe alloys is required to reliably determine ρ , calculate thermal conductivity and provide direct measurements for potential core compositions under terrestrial planetary core conditions. This further investigation is crucial for constraining ρ more accurately for likely core compositions and gaining a clearer understanding of the heat budget, the age of the inner core, and the thermal evolution of terrestrial planetary bodies as well as the likelihood of thermal convection as an energy source in a core with a dynamo.

References

- Alfè, D. (2015). The Ab Initio Treatment of High-Pressure and High-Temperature Mineral Properties and Behavior. In *Treatise on Geophysics* (pp. 369–392). Elsevier. <https://doi.org/10.1016/B978-0-444-53802-4.00040-3>.
- Basu, A., Field, M. R., McCulloch, D. G., & Boehler, R. (2020). New measurement of melting and thermal conductivity of iron close to outer core conditions. *Geoscience Frontiers*, 11(2), 565–568. <https://doi.org/10.1016/j.gsf.2019.06.007>.
- Berrada, M., & Secco, R. A. (2021). Review of Electrical Resistivity Measurements and Calculations of Fe and Fe-Alloys Relating to Planetary Cores. *Frontiers in Earth Science*, 9, 732289. <https://doi.org/10.3389/feart.2021.732289>.
- Ceperley, D. M. (2010). An Overview of Quantum Monte Carlo Methods. *Reviews in Mineralogy and Geochemistry*, 71(1), 129–135. <https://doi.org/10.2138/rmg.2010.71.6>.
- Duffy, T., Madhusudhan, N., & Lee, K. K. M. (2015). Mineralogy of Super-Earth Planets. In *Treatise on Geophysics* (pp. 149–178). Elsevier. <https://doi.org/10.1016/B978-0-444-53802-4.00053-1>.
- Hsieh, W.-P., Goncharov, A. F., Labrosse, S., Holtgrewe, N., Lobanov, S. S., Chuvashova, I., Deschamps, F., & Lin, J.-F. (2020). Low thermal conductivity of iron-silicon alloys at Earth's core conditions with implications for the geodynamo. *Nature Communications*, 11(1), 3332. <https://doi.org/10.1038/s41467-020-17106-7>.
- Ishii, T., Liu, Z., & Katsura, T. (2019). A Breakthrough in Pressure Generation by a Kawai-Type Multi-Anvil Apparatus with Tungsten Carbide Anvils. *Engineering*, 5(3), 434–440. <https://doi.org/10.1016/j.eng.2019.01.013>.
- Konôpková, Z., McWilliams, R. S., Gómez-Pérez, N., & Goncharov, A. F. (2016). Direct measurement of thermal conductivity in solid iron at planetary core conditions. *Nature*, 534(7605), 99–101. <https://doi.org/10.1038/nature18009>.
- Korell, J.-A., French, M., Steinle-Neumann, G., & Redmer, R. (2019). Paramagnetic-to-Diamagnetic Transition in Dense Liquid Iron and Its Influence on Electronic Transport Properties. *Physical Review Letters*, 122(8), 086601. <https://doi.org/10.1103/PhysRevLett.122.086601>.
- Li, J., & Fei, Y. (2014). Experimental Constraints on Core Composition. In *Treatise on Geochemistry* (pp. 527–557). Elsevier. <https://doi.org/10.1016/B978-0-08-095975-7.00214-X>.

- Li, W.-J., Li, Z., He, X.-T., Wang, C., & Zhang, P. (2021). Constraints on the thermal evolution of Earth's core from ab initio calculated transport properties of FeNi liquids. *Earth and Planetary Science Letters*, 562, 116852. <https://doi.org/10.1016/j.epsl.2021.116852>.
- Nellis, W. J. (2010). P. W. Bridgman's contributions to the foundations of shock compression of condensed matter. *Journal of Physics: Conference Series*, 215, 012144. <https://doi.org/10.1088/1742-6596/215/1/012144>.
- Oganov, A. R., Hemley, R. J., Hazen, R. M., & Jones, A. P. (2013). Structure, Bonding, and Mineralogy of Carbon at Extreme Conditions. *Reviews in Mineralogy and Geochemistry*, 75(1), 47–77. <https://doi.org/10.2138/rmg.2013.75.3>.
- Ohta, K., Kuwayama, Y., Hirose, K., Shimizu, K., & Ohishi, Y. (2016). Experimental determination of the electrical resistivity of iron at Earth's core conditions. *Nature*, 534(7605), 95–98. <https://doi.org/10.1038/nature17957>.
- Ovsyannikov, S. V., Bykov, M., Bykova, E., Kozlenko, D. P., Tsirlin, A. A., Karkin, A. E., Shchennikov, V. V., Kichanov, S. E., Gou, H., Abakumov, A. M., Egoavil, R., Verbeeck, J., McCammon, C., Dyadkin, V., Chernyshov, D., Van Smaalen, S., & Dubrovinsky, L. S. (2016). Charge-ordering transition in iron oxide Fe₄O₅ involving competing dimer and trimer formation. *Nature Chemistry*, 8(5), 501–508. <https://doi.org/10.1038/nchem.2478>.
- Poirier, J.-P. (1994). Light elements in the Earth's outer core: A critical review. *Physics of the Earth and Planetary Interiors*, 85(3–4), 319–337. [https://doi.org/10.1016/0031-9201\(94\)90120-1](https://doi.org/10.1016/0031-9201(94)90120-1).
- Pommier, A., Driscoll, P. E., Fei, Y., & Walter, M. J. (2022). Investigating metallic cores using experiments on the physical properties of liquid iron alloys. *Frontiers in Earth Science*, 10, 956971. <https://doi.org/10.3389/feart.2022.956971>.
- Pourovskii, L. V., Mravlje, J., Pozzo, M., & Alfè, D. (2020). Electronic correlations and transport in iron at Earth's core conditions. *Nature Communications*, 11(1), 4105. <https://doi.org/10.1038/s41467-020-18003-9>.
- Pozzo, M., Davies, C., Gubbins, D., & Alfè, D. (2013). Transport properties for liquid silicon-oxygen-iron mixtures at Earth's core conditions. *Physical Review B*, 87(1), 014110. <https://doi.org/10.1103/PhysRevB.87.014110>.
- Saha, P., Mazumder, A., & Mukherjee, G. D. (2020). Thermal conductivity of dense hcp iron: Direct measurements using laser heated diamond anvil cell. *Geoscience Frontiers*, 11(5), 1755–1761. <https://doi.org/10.1016/j.gsf.2019.12.010>.

- Sakai, T., Ohtani, E., Hirao, N., & Ohishi, Y. (2011). Stability field of the hcp-structure for Fe, Fe-Ni, and Fe-Ni-Si alloys up to 3 Mbar. *Geophysical Research Letters*, 38(9), 2011GL047178. <https://doi.org/10.1029/2011GL047178>.
- Seagle, C. T., Cottrell, E., Fei, Y., Hummer, D. R., & Prakapenka, V. B. (2013). Electrical and thermal transport properties of iron and iron-silicon alloy at high pressure: TRANSPORT PROPERTIES OF Fe AND Fe-Si. *Geophysical Research Letters*, 40(20), 5377–5381. <https://doi.org/10.1002/2013GL057930>.
- Swift, D., Eggert, J., Hicks, D., Hamel, S., Caspersen, K., Schwegler, E., Collins, G., Nettelmann, N., & Ackland, G. (2012). Mass-radius relationships for exoplanets. *The Astrophysical Journal*, 744(1), 59. <https://doi.org/10.1088/0004-637X/744/1/59>.
- Tateno, S., Hirose, K., Ohishi, Y., and Tatsumi, Y. (2010) The Structure of Iron in Earth's Inner Core. *Science*, 330(6002), 359 LP – 361. <https://doi.org/10.1126/science.1194662>.
- Terasaki, H., Kamada, S., Sakai, T., Ohtani, E., Hirao, N., & Ohishi, Y. (2011). Liquidus and solidus temperatures of a Fe–O–S alloy up to the pressures of the outer core: Implication for the thermal structure of the Earth's core. *Earth and Planetary Science Letters*, 304(3–4), 559–564. <https://doi.org/10.1016/j.epsl.2011.02.041>.
- Wagle, F., Steinle-Neumann, G., & De Koker, N. (2019). Resistivity saturation in liquid iron–light-element alloys at conditions of planetary cores from first principles computations. *Comptes Rendus Geoscience*, 351(2–3), 154–162. <https://doi.org/10.1016/j.crte.2018.05.002>.
- Xu, J., Zhang, P., Haule, K., Minar, J., Wimmer, S., Ebert, H., & Cohen, R. E. (2018). Thermal Conductivity and Electrical Resistivity of Solid Iron at Earth's Core Conditions from First Principles. *Physical Review Letters*, 121(9), 096601. <https://doi.org/10.1103/PhysRevLett.121.096601>.
- Yin, Y., Zhang, Q., Zhang, Y., Zhai, S., & Liu, Y. (2022). Electrical and thermal conductivity of Earth's core and its thermal evolution—A review. *Acta Geochimica*, 41(4), 665–688. <https://doi.org/10.1007/s11631-021-00523-w>.
- Zhai, S., & Ito, E. (2011). Recent advances of high-pressure generation in a multianvil apparatus using sintered diamond anvils. *Geoscience Frontiers*, 2(1), 101–106. <https://doi.org/10.1016/j.gsf.2010.09.005>.
- Zhang, L., & Fei, Y. (2008). Melting behavior of (Mg,Fe)O solid solutions at high pressure. *Geophysical Research Letters*, 35(13), L13302. <https://doi.org/10.1029/2008GL034585>.
- Zhang, Y., Hou, M., Liu, G., Zhang, C., Prakapenka, V. B., Greenberg, E., Fei, Y., Cohen, R. E., & Lin, J.-F. (2020). Reconciliation of Experiments and Theory on

Transport Properties of Iron and the Geodynamo. *Physical Review Letters*, 125(7), 078501. <https://doi.org/10.1103/PhysRevLett.125.078501>.

Zidane, M., Salmani, E. M., Majumdar, A., Ez-Zahraouy, H., Benyoussef, A., & Ahuja, R. (2020). Electrical and thermal transport properties of Fe–Ni based ternary alloys in the earth's inner core: An ab initio study. *Physics of the Earth and Planetary Interiors*, 301, 106465. <https://doi.org/10.1016/j.pepi.2020.106465>.

Chapter 3

3 Thermal convection in Vesta's core from experimentally based conductive heat flow estimates

A version of this chapter has been published (Orole, O. A., Yong, W., & Secco, R. A. (2022). Thermal Convection in Vesta's Core from Experimentally Based Conductive Heat Flow Estimates. *Crystals*, 12(12), 1752. <https://doi.org/10.3390/cryst12121752>.

3.1 Introduction

Most terrestrial planets possess a core composed of a solid inner core and a liquid outer core. Flow of liquid in the outer core results in the generation of an internal magnetic field on terrestrial bodies (Roberts, 1968). A major energy source of fluid motion is thermal convection which is active when thermal conduction, or outer core adiabatic heat flow, is insufficient to provide the heat required to traverse the CMB. From models of core evolution for the best-studied planet, Earth, the evolutionary pathways of terrestrial bodies during cooling are directly influenced by the thermal conductivity of the Fe alloys comprising their cores. Results from previous experimental studies (Berrada et al., 2022; Berrada et al., 2021; Gomi and Hirose, 2015; Littleton et al., 2021a; Littleton et al., 2021b; Pommier et al., 2020; Berrada et al., 2020; Yong et al., 2019; Silber et al., 2019; Silber et al., 2018; Zhang et al., 2021; Pommier, 2017; Secco, 2017; Ezenwa and Secco, 2017; Gomi et al., 2016; Ho et al., 1983) indicate that thermal conductivity of Fe alloys is dependent on P and T. In order to determine the adiabatic heat flow inside the liquid core of a terrestrial body, effects of P and T on thermal conductivity of core-mimetic alloys must be known. Comparing the determined adiabatic heat flow with a knowledge of the heat flow through the CMB, the likelihood of thermal convection can be assessed.

The results of the experiments carried out in this study are applied to understand the core dynamics of the asteroid 4-Vesta. As the second largest asteroid with a diameter of 525 km, Vesta is located in the main asteroid belt, is differentiated with a metallic core, and is thought to have emerged during the early formation of our solar system (McSween and Huss, 2010). Although Vesta's core has been assumed to be composed of pure Fe (Formisano et al., 2016), by comparing Howardite-Eucrite-Diogenite (HED) and

chondritic meteorites (Dreibus et al., 1997), Vesta's core composition is estimated to contain ~92% Fe and ~8% Ni. HED meteorites are assumed to have been ejected from Vesta because they share similar properties such as comparative mineralogy and spectral reflectivity with Vesta (McCord et al., 1970; Russell et al., 2012).

Presently, Vesta does not possess a magnetic field but paleomagnetic studies performed on the meteorites from Vesta indicate that as far back as 3.69 billion years ago, the surface of Vesta had a magnetic field intensity of 2 μ T from an internally generated magnetic field (Fu et al., 2012). By comparison with other core-generated magnetic fields in terrestrial-type planetary bodies, the generation of Vesta's past core dynamo is most likely a result of the motion of the liquid outer core caused by either compositional convection and/or thermal convection. Thermal convection could have stirred Vesta's liquid outer core at any time in the past, as long as heat transfer through the CMB from the liquid core exceeded the adiabatic heat flow in the core. The primary condition for compositional convection to help drive Vesta's dynamo is the presence of a solid Fe-rich inner core from which light alloying elements, dispelled into the fluid on inner core solidification, provide the buoyancy force for outward radial fluid movement (Ho et al., 1983).

The goal of this study is to assess whether thermal convection in Vesta's liquid outer core could have once powered its dynamo. The contribution of thermal convection to the total heat flow at the top of the liquid region of Vesta's core is estimated by comparing the conductive heat flux at the top of its core with the estimates of heat flow across its CMB. The conductive heat flux is derived from the thermal conductivity which is calculated from the experimentally measured electrical resistivity of Fe-5 wt% Ni in this study.

3.2 Methods

A wire-shaped sample of Fe-5 wt% Ni (custom purchase from chemPUR, 99.9% purity) was assembled into a cubic pressure cell and placed in a 1000-ton cubic anvil press. The sample was heated by passing a high alternating current of up to ~250 A through a cylindrical graphite furnace after the pressure had stabilized at the target value. As shown in Figure 3.1, the four-wire electrode method was used.

The electrodes were made of thermocouples of 95W5Re and 74W26Re wires (Type C thermocouple) so that in thermocouple mode, temperature measurements were made and in resistance mode, voltage drop measurement was made by propagating a constant current of 0.2 A, from a Keysight B2961A power source through two of the electrodes. A platinum (Pt) disc was used in the cell assembly to increase the contact between the sample and the thermocouple/electrodes and to delay the contamination of the thermocouple to ensure more accurate temperature readings.

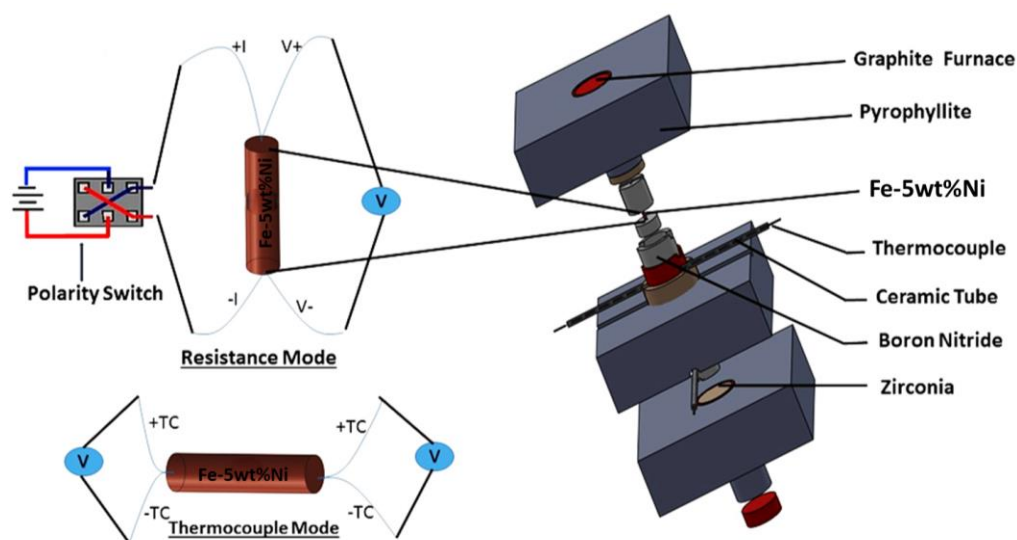


Figure 3.1: Schematic diagram of cell design (modified from Ezenwa and Secco, 2017).

A preheating run up to ~ 1023 K followed by quenching in each experiment guaranteed that all metal components of the experimental setup were in good contact. After the preheating run, resistivity measurements were made on heating from room temperature to the final run temperature. Temperature was then quenched by shutting off the power to the furnace. A current polarity switch was used to eliminate any parasitic potentials and to obtain several voltage readings for both negative and positive currents at a given temperature.

The resistivity of Fe-5 wt% Ni as a function of temperature and pressure was determined from averaging ~ 10 voltage readings taken by a Keysight 34470A data acquisition meter

operating at 20 Hz, into a single data point per temperature value. Ohm's and Pouillet's laws were used to propagate the observed voltage error value (standard deviation of the voltage measurements) using the standard of formalism of Bevington and Robinson (Bevington and Robinson, 2003).

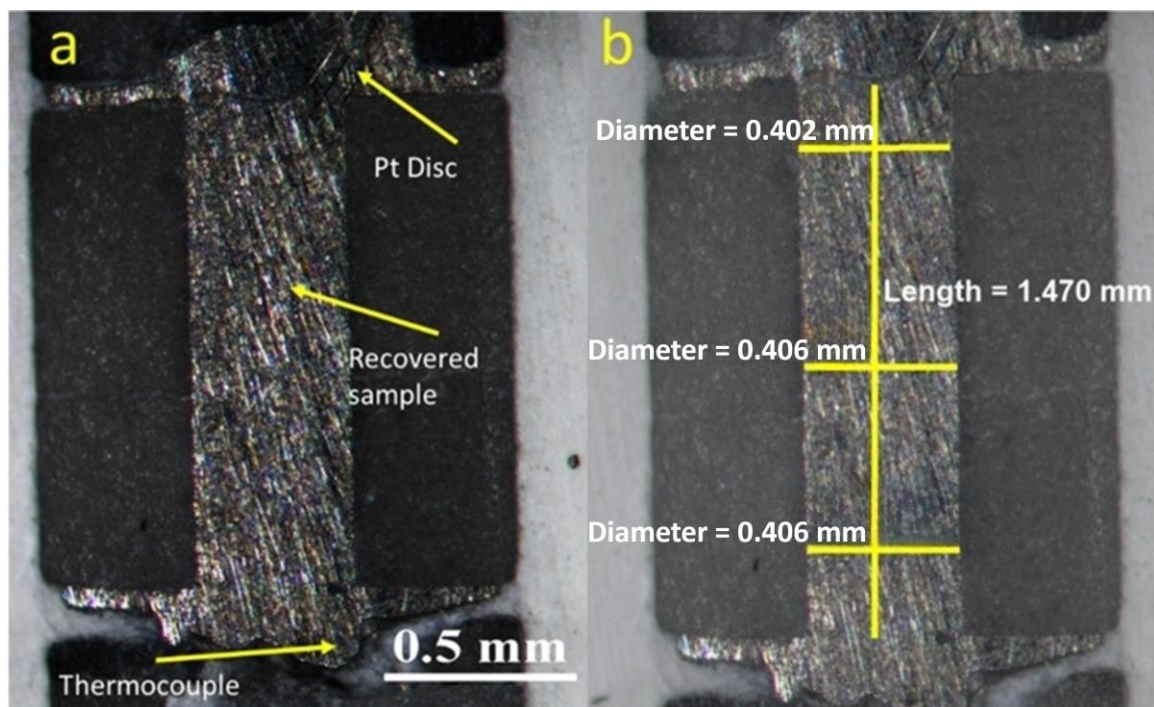


Figure 3.2: Cross sectional image of Fe-5 wt% Ni recovered from 4 GPa and 1986 K (a) Cross sectional image of a polishing stage of the sample (b) Cross sectional image of a polishing stage of the sample with the value for the length and diameter recorded.

By measuring the electrical resistivity of Fe-5 wt% Ni at pressures of 2–5 GPa and temperatures into the liquid state, thermal conductivity of Fe-5 wt% Ni was calculated from electrical resistivity using the Wiedemann Franz law, $\kappa = LT/\rho$ (Wiedemann and Franz, 1853) where ρ is the electrical resistivity at a specific P and T, L is the Lorenz number (with a theoretically calculated Sommerfeld value, L_0 , of $2.445 \times 10^{-8} \text{ W}\Omega\text{K}^{-2}$) and κ is thermal conductivity.

The recovered pressure cell assembly after each experimental run was dismantled to retrieve the boron nitride sleeve housing the sample. A Nikon SMZ800 microscope was

used to take photographs of each polishing stage of the sample as shown in Figure 3.2a and the value for the length and diameter of the sample at each polishing stage were recorded on the cross-section photographs as shown in Figure 3.2b. After reaching the center of the sample, the polished cross-section was encased in epoxy prior to an electron microprobe analysis (EMPA) of its chemical composition using the JEOL JXA-8530F field-emission electron microprobe manufactured by JEOL Ltd in Tokyo, Japan with a 50 nA probe current, 20 kV accelerating voltage, and 10 μm spot-size beam.

3.3 Results

Post-experimental analysis indicated that the sample retained its cylindrical geometry and was well-contained even at temperatures into the liquid state, as shown in Figure 3.2.

Progressive contamination of Pt from the disc into the sample occurs at higher temperatures above the melting temperature. The highest temperature experimental runs were heated to ~ 270 K above melting and at these high temperatures, there is significant contamination from Pt. To understand at what temperature Pt contamination in the sample started, tests were conducted in two separate runs at 4 GPa at the following temperature conditions: 55 K below melting temperature followed by quenching, 54 K above melting temperature followed by quenching. Both samples were recovered, analyzed and compared with the EMPA analysis of the 4 GPa resistivity run that was heated to 193 K above the melting temperature as shown in Figure 3.3a–c. The compositions for the recovered sample quenched at 55 K below the melting temperature (Figure 3.3a) shows that there is no contamination for temperature up to the melting temperature. The recovered sample that was quenched at 54 K above the melting temperature (Figure 3.3b) shows that contamination starts after melting and the amount of contamination is dependent on temperature, and thus time duration in the liquid state as shown in Figure 3.3b,c. Our calculation of thermal conductivity, from which core adiabatic heat flow is derived, relies on the resistivity value at the melting temperature. On the basis of these contamination test runs, this ensures that the sample is uncontaminated in the solid state and early liquid state and the resistivity values used represent values for Fe-5 wt% Ni.

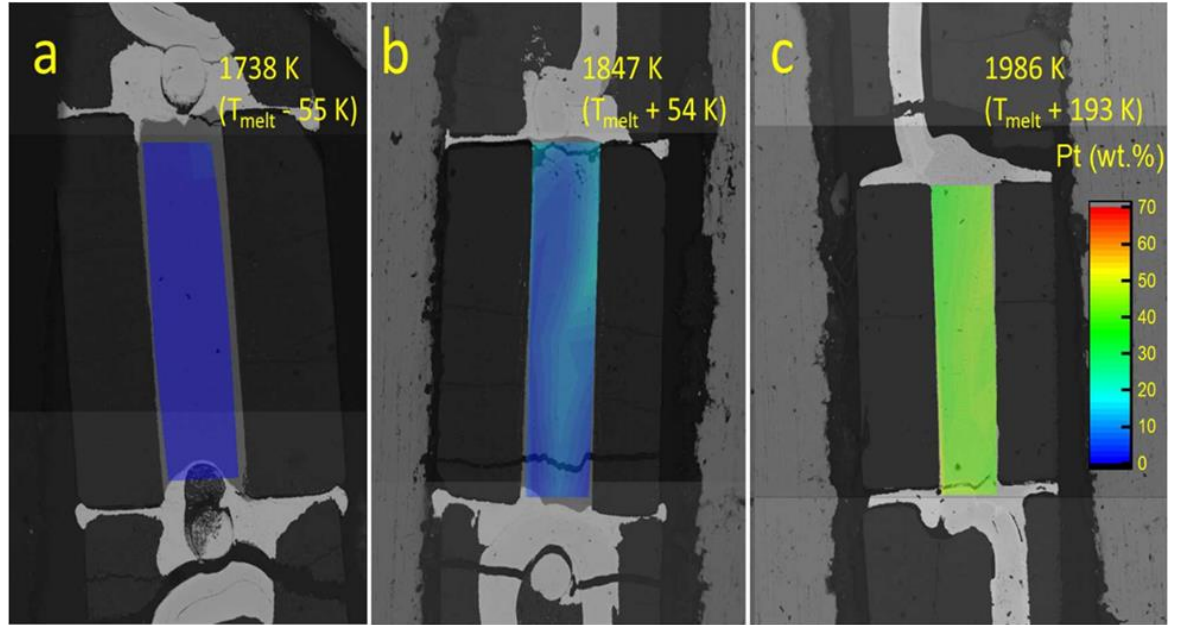


Figure 3.3: Chemical composition of Fe-5 wt% Ni recovered from three separate experiments at 4 GPa that reached maximum T of: (a) 1738 K ($T_{\text{melt}} - 55$ K); (b) 1847 K ($T_{\text{melt}} + 54$ K); and (c) 1986 K ($T_{\text{melt}} + 193$ K).

Figure 3.4 shows the electrical resistivity of Fe-5 wt% Ni as a function of temperature at pressures of 2–5 GPa. The magnetic transition at ~ 900 K and the melting at ~ 1800 K are visible on the plot. The noticeable similarities in the trends of the 2, 3, 4 and 5 GPa data indicate internal consistency and reproducibility. The thermal conductivity of Fe-5 wt% Ni was calculated using the Wiedemann Franz law. Although the Lorenz number may vary with pressure and temperature, this study uses the Sommerfeld value as a representative value of the Lorenz number (Zhang et al., 2021) to calculate the thermal conductivity of Fe-5 wt% Ni since we are not aware of a specific Lorenz value for Fe-5 wt% Ni. The thermal conductivity plot, given in Figure 3.5, shows a sudden increase at the magnetic transition (~ 900 K) of Fe-5 wt% Ni and a decrease of thermal conductivity on melting.

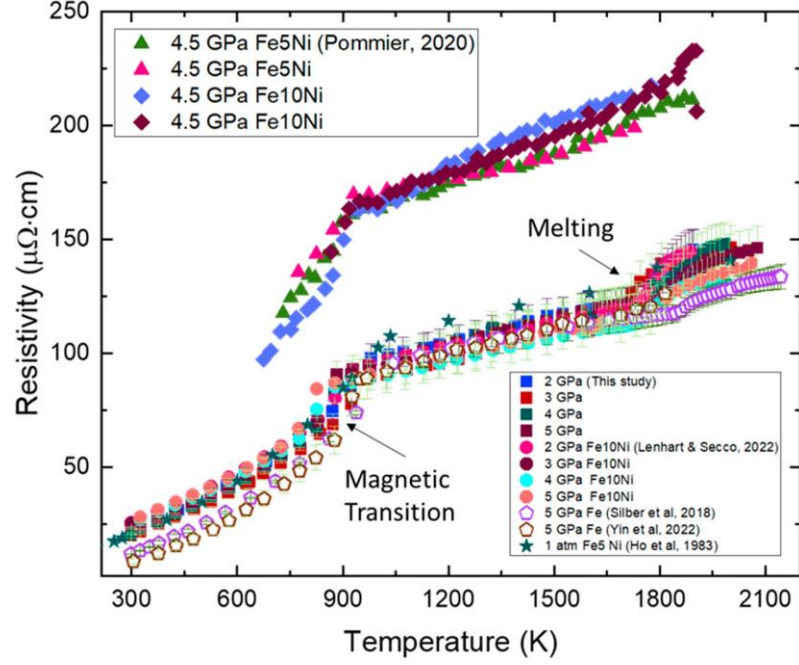


Figure 3.4: Comparison of the electrical resistivity of Fe-5 wt% Ni and Fe-10 wt% Ni (Silber et al., 2018; Ho et al.,1983; Lenhart and Secco, 2022; Pommier, 2020; Yin et al., 2022).

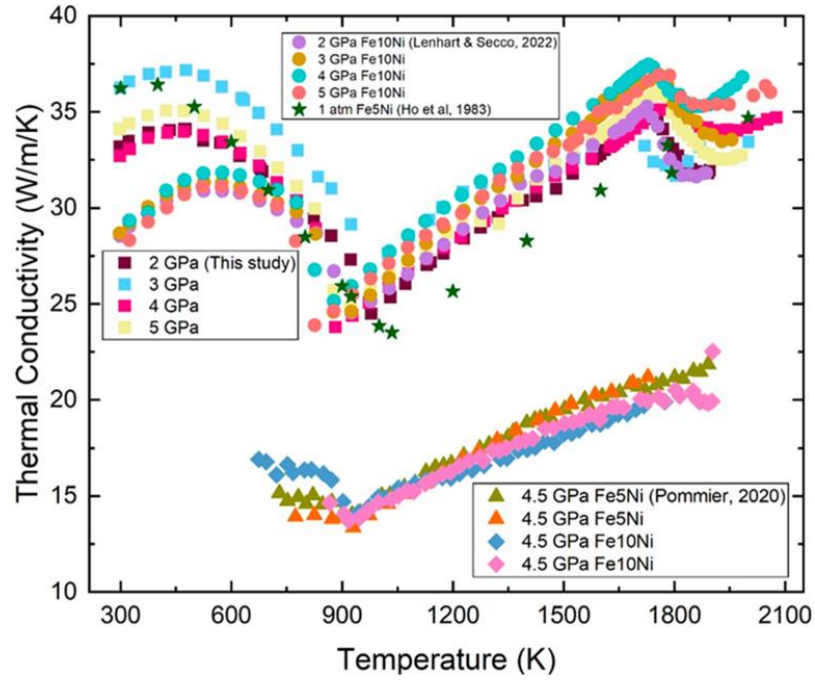


Figure 3.5: Comparison of thermal conductivity of Fe-5 wt% Ni and Fe-10 wt% Ni (Ho et al.,1983; Lenhart and Secco, 2022; Pommier, 2020).

3.4 Discussion

From Figures 3.4 and 3.5, there are noticeable similarities in the trends of the results for this study and those of previous studies (Ho et al., 1983; Lenhart and Secco, 2022; Pommier, 2020) with similar sample composition. The expected trend of decreasing resistivity with increasing pressure can be seen in the high temperature region when comparing the data from this study to the 1 atm data from Ho et al. (1983). The dataset by Pommier, (2020) shows the opposite trend. Comparison of the electrical resistivity and thermal conductivity data (Figures 3.4 and 3.5) of Fe-5 wt% Ni from this study with Fe-10 wt% Ni from Lenhart and Secco, (2020); and separate comparison of the Fe-5 wt% Ni with Fe-10 wt% Ni from Pommier, (2020) indicates that the change in the Ni content of up to 10 wt% has no significant effect on the electrical resistivity and thermal conductivity values of Fe-Ni alloys.

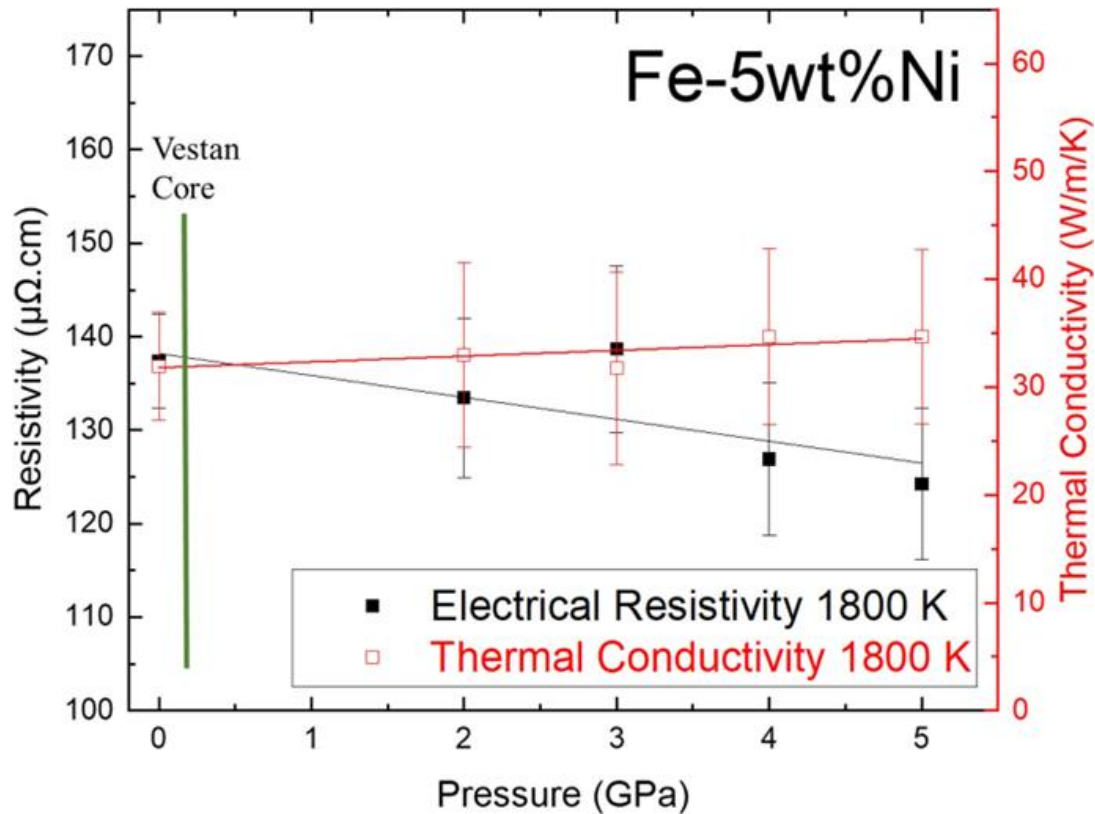


Figure 3.6: High pressure electrical resistivity and thermal conductivity data at 1800 K from this study plotted with 1 atm data (Ho et al., 1983) for purpose of interpolation to Vestan CMB pressure of 0.2 GPa.

Figure 3.6 shows the measured electrical resistivity and calculated thermal conductivity data at 1800 K and high pressures from this study plotted with 1 atm data, (1983) at 1800 K for the purpose of interpolation to Vestan CMB pressure of 0.2 GPa. At 1 atm, the resistivity datum was measured, (1983) and thermal conductivity was calculated in the same way as for the high-pressure data. The ideal Lorenz number (L_o) was used in the calculations for this study because the exact value for the Lorenz number for Fe-5 wt% Ni is unknown. Since our composition is 95 wt% Fe, our use of L_o is consistent with the calculated values of L/L_o that show a variation of 1.01–1.06 along the melting boundary of pure Fe in the pressure range 2–5 GPa (Secco, 2017). This approach is also consistent with the conclusions of another study that states that the Sommerfeld value is a good approximation for terrestrial cores (Gomi and Hirose, 2015).

The trend lines shown in Figure 3.6 between the ambient pressure data from Ho et al, (1983) and this study (2–5 GPa) supports the interpolation of electrical resistivity and thermal conductivity at pressure values in Vesta's core. The estimated pressure at Vesta's center (0.2–0.3 GPa) is approximately double the pressure at Vesta's CMB (0.1–0.2 GPa) (McSween and Huss, 2010). The adiabatic heat flux at the top of Vesta's core is estimated by using the thermal conductivity value of Fe-5 wt% Ni at each pressure just after melting: (2 GPa, 32.6 W/m/K), (3 GPa, 33.7 W/m/K), (4 GPa, 33.2 W/m/K), (5 GPa, 33.4 W/m/K) and the thermal conductivity value for Fe-5 wt% Ni at ambient pressure just after melting (Ho et al) to interpolate to 0.2 GPa the thermal conductivity value of Fe-5 wt% Ni ($\kappa = 34.1$ W/m/K).

The adiabatic heat flux density (~ 2.2 mW/m²) was calculated using Fourier's law for heat transfer $q = -\kappa \nabla T$, where $\kappa = 34.1$ W/m/K and the temperature gradient in the core, $\nabla T = -0.06$ K/km from the equation $\nabla T = -\alpha g T / C_p$ when α (thermal expansion coefficient) is 10^{-4} K⁻¹, g (gravitational acceleration) is 0.3 m/s², T is 1700 K and C_p (isobaric heat capacity) is 800 J kg⁻¹ K⁻¹ (Lenhart and Secco, 2022).

Using the equation $Q_{ad} = -4\pi r^2 \kappa \nabla T$ and radius $r = 110$ km (under the assumption of radial symmetry), the total adiabatic heat flux at the top of Vesta's core is ~ 331 MW. The estimated adiabatic heat flux density of ~ 2.2 mW/m² and the heat flow of ~ 331 MW at

the top of Vesta's early core in this study are much smaller than the estimated heat flux density of 10–500 mW/m² and the corresponding heat flow of ~1.5–78 GW through Vesta's early CMB (Ho et al., 1983; Weiss et al., 2010). Since the calculated adiabatic heat flow is very much smaller than the heat flow through the CMB, thermal convection is necessary to transport heat within the core to the CMB. This indicates the strong likelihood that the mechanism stirring Vesta's liquid outer core to generate its surface magnetic field for tens of millions of years in its early history was thermal convection.

The estimated values of adiabatic heat flow in the core from this study are based on thermal conductivity values calculated from our electrical resistivity measurements while the estimated heat flow values through Vesta's early CMB are from modelling in previous studies. The accuracy of these two approaches is dependent on other parameters like the temperature gradient inside Vesta, and some of these parameters are not well constrained. Apart from Ni in Vesta's core, some authors propose (Zhang et al., 2020; Wu et al., 2018) the presence of other light elements like S and Si. Although the range of increase to the electrical resistivity is uncertain, S increases the electrical resistivity of the Fe alloy melt at high pressures (Littleton et al., 2021a; Pommier, 2017). The presence of S infers a lower density estimate for an Fe-S core which increases the estimated characteristic length because a higher core radius will be derived from the gravitational study of Russell et al., (2012). The presence of small amount of Si does not change the electrical resistivity of liquid Fe as indicated by the study done by Silber et al., (2019) on Fe-4.5 wt% Si which shows that the electrical resistivity of liquid Fe alloys is constant along the melting curve and also similar to the electrical resistivity of pure Fe.

3.5 Conclusions

Comparing the result of this study with those of pure Fe and Fe-10 wt% Ni (Zhang et al., 2021; Ho et al., 1983; Lenhart and Secco, 2022; Pommier, 2020) at similar pressures shows that at high temperatures, Ni contents of up to 10 wt% in pure liquid Fe does not significantly increase the electrical resistivity. Therefore, thermal convection is the most likely energy source mechanism for Vesta's past core dynamo because the estimated adiabatic heat flux density of ~2.2 mW/m² at the top of Vesta's early core is much smaller than the heat flux density estimates across Vesta's early CMB.

References

- Berrada, M., Secco, R. A., & Yong, W. (2022). Resistivity of solid and liquid Fe–Ni–Si with applications to the cores of Earth, Mercury and Venus. *Scientific Reports*, 12, Article 1.
- Berrada, M., Secco, R. A., & Yong, W. (2021). Adiabatic heat flow in Mercury’s core from electrical resistivity measurements of liquid Fe-8.5 wt%Si to 24 GPa. *Earth and Planetary Science Letters*, 568, 117053.
- Berrada, M., Secco, R. A., Yong, W., & Littleton, J. A. H. (2020). Electrical Resistivity Measurements of Fe-Si with Implications for the Early Lunar Dynamo. *Journal of Geophysical Research: Planets*, 125.
- Bevington, P. R., & Robinson, D. K. (2003). *Data Reduction and Error Analysis*. McGraw-Hill.
- Dreibus, G., Bruckner, J., & Wanke, H. (1997). On the core mass of the asteroid Vesta. *Meteorite. Planet. Sci.*, 32, 36.
- Ezenwa, I. C., & Secco, R. A. (2017). Constant electrical resistivity of Zn along the melting boundary up to 5 GPa. *High Pressure Research*, 37(3), 319–333.
- Ezenwa, I. C., Secco, R. A., Yong, W., Pozzo, M., & Alfè, D. (2017). Electrical resistivity of solid and liquid Cu up to 5 GPa: Decrease along the melting boundary.
- Formisano, M., Federico, C., Angelis, S., Sanctis, M. C., & Magni, G. (2016). A core dynamo in Vesta? *Monthly Notices of the Royal Astronomical Society*, 458, 695–707.
- Fu, R. R., Weiss, B. P., Shuster, D. L., Gattacceca, J., Grove, T. L., Suavet, C., Lima, E. A., Li, L., & Kuan, A. T. (2012). An Ancient Core Dynamo in Asteroid Vesta. *Science*, 338(6104), 238–241.
- Gomi, H., & Hirose, K. (2015). Electrical resistivity and thermal conductivity of hcp Fe–Ni alloys under high pressure: Implications for thermal convection in the Earth’s core. *Physics of the Earth and Planetary Interiors*, 247, 2–10.
- Gomi, H., Hirose, K., Akai, H., & Fei, Y. (2016). Electrical resistivity of substitutionally disordered hcp Fe–Si and Fe–Ni alloys: Chemically-induced resistivity saturation in the Earth’s core. *Earth and Planetary Science Letters*, 451, 51–61.
- Ho, C. Y., Ackerman, M. W., Wu, K. Y., Havill, T. N., Bogaard, R. H., Matula, R. A., Oh, S. G., & James, H. M. (1983). Electrical Resistivity of Ten Selected Binary Alloy Systems. *Journal of Physical and Chemical Reference Data*, 12(2), Article 2.

- Lenhart, E. M., & Secco, R. A. (2022). Implications for the energy source for an early dynamo in Vesta from experiments on electrical resistivity of liquid Fe-5wt%Ni at high pressures. *Icarus*, 114962.
- Littleton, J. A. H., Secco, R. A., & Yong, W. (2021a). Thermal Convection in the Core of Ganymede Inferred from Liquid Eutectic Fe-FeS Electrical Resistivity at High Pressures. *Crystals*, 11(8), 875.
- Littleton, J. A. H., Secco, R. A., & Yong, W. (2021b). Electrical Resistivity of FeS at High Pressures and Temperatures: Implications of Thermal Transport in the Core of Ganymede. *Journal of Geophysical Research: Planets*, 126(5), Article 5.
- McCord, T. B., Adams, J. B., & Johnson, T. V. (1970). Asteroid Vesta: Spectral reflectivity and compositional implications. *Science*, 168, 1445–1447.
- McSween, H. Y., & Huss, G. R. (2010). *Cosmo chemistry*. Cambridge Univ. Press.
- Pommier, A. (2018). Influence of sulfur on the electrical resistivity of a crystallizing core in small terrestrial bodies. *Earth and Planetary Science Letters*, 496, 37–46.
- Pommier, A. (2020). Experimental investigation of the effect of nickel on the electrical resistivity of Fe-Ni and Fe-Ni-S alloys under pressure *American Mineralogist* (Vol. 105, Issue 7, pp. 1069–1077).
- Pommier, A., Davies, C. J., & Zhang, R. (2020). A joint experimental-modeling investigation of the effect of light elements on dynamos in small planets and moons. *Journal of Geophysical Research: Planets*, 125, 2020 006492.
- Roberts, P. H. (1968). On the thermal instability of a rotating-fluid sphere containing sources. *Philos. Tran. R. Soc. Lond. A*, 263, 93–117.
- Russell, C. T., Raymond, C. A., Coradini, A., McSween, H. Y., Zuber, M. T., Nathues, A., De Sanctis, M. C., Jaumann, R., Konopliv, A. S., Preusker, F., Asmar, S. W., Park, R. S., Gaskell, R., Keller, H. U., Mottola, S., Roatsch, T., Scully, J. E. C., Smith, D. E., Tricarico, P., ... Titus, T. N. (2012). Dawn at Vesta: Testing the Protoplanetary Paradigm. *Science*, 336(6082), 684–686.
- Secco, R. A. (2017). Thermal conductivity and Seebeck coefficient of Fe and Fe-Si alloys: Implications for variable Lorenz number. *Physics of the Earth and Planetary Interiors*, 265, 23–34.
- Silber, R. E., Secco, R. A., Yong, W., & Littleton, J. A. H. (2018). Electrical resistivity of liquid Fe to 12 GPa: Implications for heat flow in cores of terrestrial bodies. *Scientific Reports*, 8(1), Article 1.

- Silber, R. E., Secco, R. A., Yong, W., & Littleton, J. A. H. (2019). Heat Flow in Earth's Core from Invariant Electrical Resistivity of Fe-Si on the Melting Boundary to 9 GPa: Do Light Elements Matter? *Journal of Geophysical Research: Solid Earth*, 124(6), Article 6.
- Weiss, B. P., Gattacceca, J., Stanley, S., Rochette, P., & Christensen, U. R. (2010). Paleomagnetic Records of Meteorites and Early Planetesimal Differentiation. *Space Science Reviews*, 152(1–4), 341–390.
- Wiedemann, D., & Franz, R. (1853). Über die Warme-Leitungsfähigkeit der Metalle. *Ann. Phys*, 165, 497–531.
- Wu, N., Farquhar, J., Dottin, J. W., & Magalhães, N. (2018). Sulfur isotope signatures of eucrites and diogenites. *Geochimica et Cosmochimica Acta*, 233, 1–13.
- Yin, Y., Wang, L., Zhai, S., & Fei, Y. (2022). Electrical Resistivity of Fe and Fe-3 Wt%P at 5 GPa With Implications for the Moon's Core Conductivity and Dynamo. *Journal of Geophysical Research: Planets*, 127(4), Article 4.
- Yong, W., Secco, R. A., Littleton, J. A. H., & Silber, R. E. (2019). The Iron Invariance: Implications for Thermal Convection in Earth's Core. *Geophysical Research Letters*, 46(20), 11065–11070.
- Zhang, A.-C., Kawasaki, N., Bao, H., Liu, J., Qin, L., Kuroda, M., Gao, J.-F., Chen, L.-H., He, Y., Sakamoto, N., & Yurimoto, H. (2020). Evidence of metasomatism in the interior of Vesta. *Nature Communications*, 11(1), 1289.
- Zhang, Y., Hou, M., Driscoll, P., Salke, N. P., Liu, J., Greenberg, E., Prakapenka, V. B., & Lin, J.-F. (2021). Transport properties of Fe-Ni-Si alloys at Earth's core conditions: Insight into the viability of thermal and compositional convection. *Earth and Planetary Science Letters*, 553, 116614.

Chapter 4

4 Conclusion

4.1 Summary

Using a 1000-ton cubic anvil press, experiments to measure the electrical resistivity within the pressure range of 2-5 GPa and temperature range 300-2000 K were conducted on Fe₅Ni. The optical microscopy analysis of the recovered samples from each experiment indicated that the sample remained contained and maintained its cylindrical shape even when reaching liquid state temperatures. The abrupt changes in slope observed in the electrical resistivity data show the magnetic transition at ~900 K, and the melting point at ~1800 K.

EPMA of the recovered samples from the contamination experiments shows that contamination starts after melting, with the amount of contamination dependent on maximum temperature reached and duration in the liquid state. The contamination experiments provide assurance that the sample remains free from contamination during the solid state and initial stages of the liquid state indicating that the resistivity values measured, and then utilized for thermal conductivity calculations, accurately reflect the values for Fe₅Ni.

The Wiedemann-Franz law was used to calculate the thermal conductivity of Fe₅Ni, based on the electrical resistivity measurements, using the Sommerfeld value for the Lorenz number. Within the measured temperature range for each pressure, the data reveal a sharp increase in the thermal conductivity at the magnetic transition (~900 K) and a decrease at the melting temperature of Fe₅Ni.

Comparing the results of this study with previous studies on the electrical resistivity and thermal conductivity in Fe-Ni alloys provides valuable information on Vesta's thermal evolution. The adiabatic heat flow at the top of Vesta's core, as determined in this study based on the calculated thermal conductivity values, is approximately 331 MW. However, this value is significantly smaller than the estimated heat flow through Vesta's

early CMB. Since the calculated adiabatic heat flow is much smaller than the heat flow through the CMB, it suggests that thermal convection was necessary to transfer heat from the core to the CMB. This finding strongly indicates that thermal convection played a crucial role in stirring Vesta's liquid outer core, generating its surface magnetic field for millions of years during its early history.

4.2 Suggestions for Future Research

Determining the thermal properties, specifically thermal conductivity of Fe and Fe alloys at terrestrial planetary core conditions is challenging. Although there are promising experimental advancements in measuring thermal conductivity, most of the available literature on electrical resistivity and thermal conductivity of terrestrial planetary core conditions primarily focuses on pure Fe and single light element Fe alloy systems.

There is a need to adopt a methodical approach towards investigating multi-element Fe alloy systems involving light elements, like binary, ternary, and quaternary systems. Exploring the effect of various light elements like Ni, S and Si at various weight percentages, on the electrical resistivity and thermal conductivity of Fe near melting temperatures using experimental and theoretical approaches and understanding the impact of each additional element is crucial. This systematic approach is valuable because research indicates that terrestrial planetary cores are unlikely to consist solely of a single light element. Ternary systems which better mimic the core compositions of terrestrial planetary bodies can be investigated by combining Ni, which has a lower electrical resistivity than Fe, with light elements in high pressure and temperature experiments, this will lead to intriguing outcomes that hold the potential to provide insights into the thermal evolution of terrestrial planetary bodies.

Additionally, resolving the issue of sample contamination at high temperatures will enhance the experimental approaches utilized and the data obtained. This problem can be addressed with the use of alternative discs, such as Rhenium (Re) and Tungsten (W), for the sample cell assembly.

Furthermore, thermal conductivity measurements are very difficult to make but a larger set of experimentally acquired data are needed to validate the use of electrical resistivity data for calculating thermal conductivity. This will help to corroborate the theoretically determined Lorenz numbers at high P and T conditions.

Appendices

Appendix A: Additional Cross Sectional Images and EMPA Results

A.1 Additional Cross Sectional Images

The figures below display additional cross sectional images of the polishing stage for different recovered samples, illustrating the progress of the polishing process with time. The length and diameter of the samples were measured and recorded with a digital camera installed on the Nikon SMZ800 microscope.



Figure A.1.1: Cross sectional image of the initial polishing stage of Fe-5 wt% Ni recovered from 2 GPa and 1896 K.

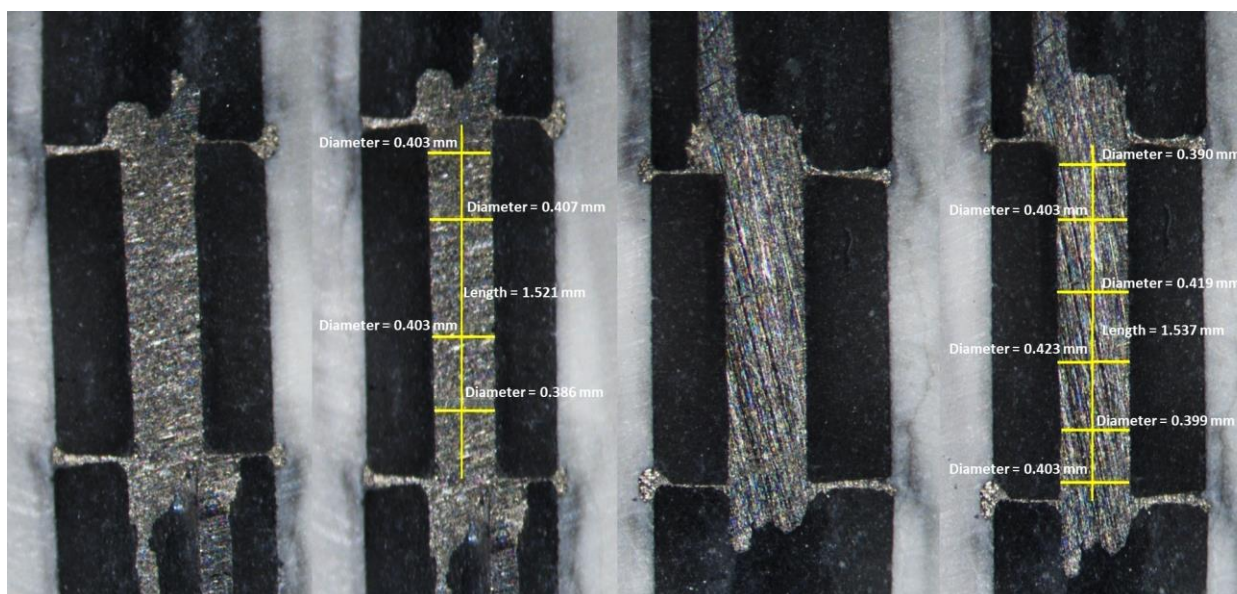


Figure A.1.2: Cross sectional image of the middle polishing stage of Fe-5 wt% Ni recovered from 2 GPa and 1896 K.

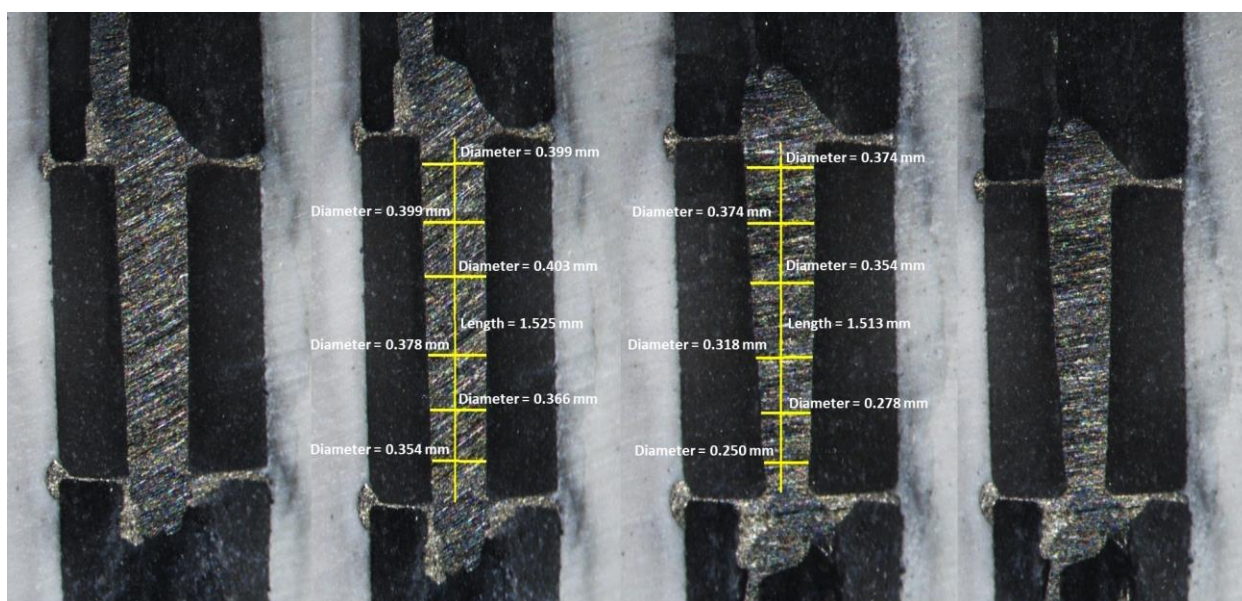


Figure A.1.3: Cross sectional image of the end polishing stage of Fe-5 wt% Ni recovered from 2 GPa and 1896 K.

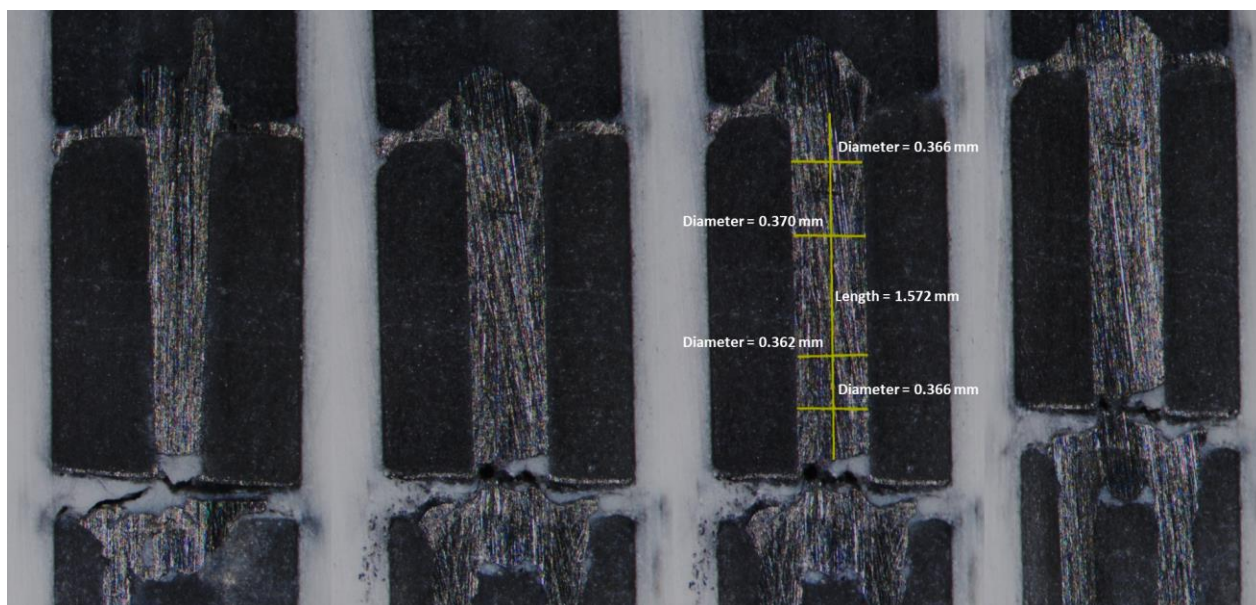


Figure A.1.4: Cross sectional image of the initial polishing stage of Fe-5 wt% Ni recovered from 3 GPa and 1960 K.

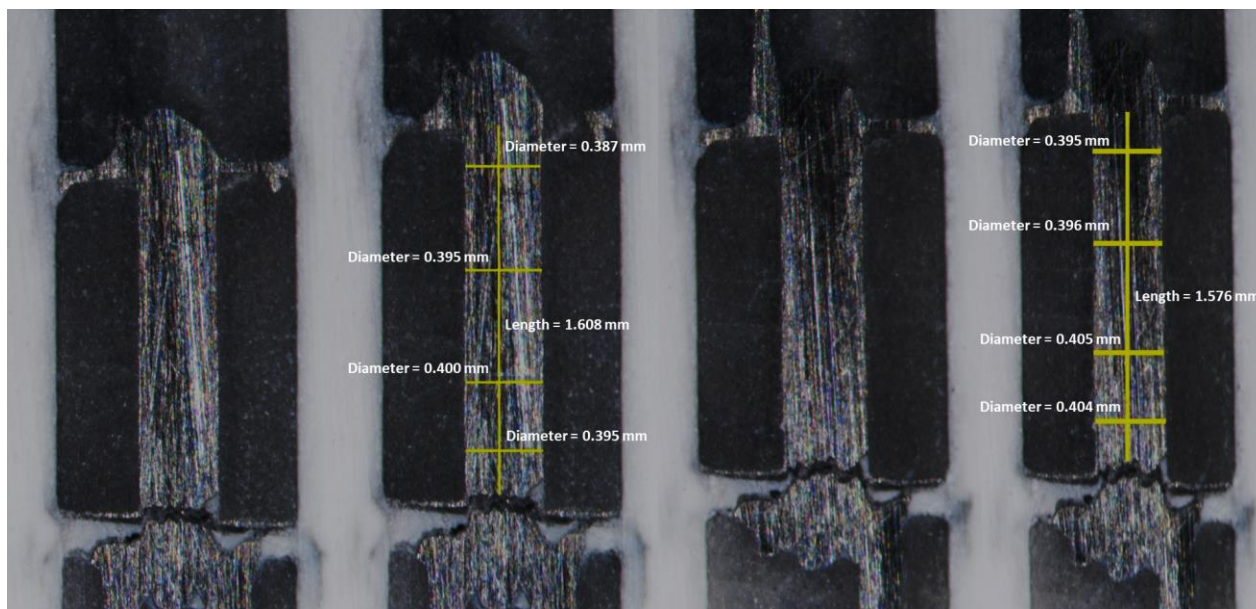


Figure A.1.5: Cross sectional image of the middle polishing stage of Fe-5 wt% Ni recovered from 3 GPa and 1960 K.

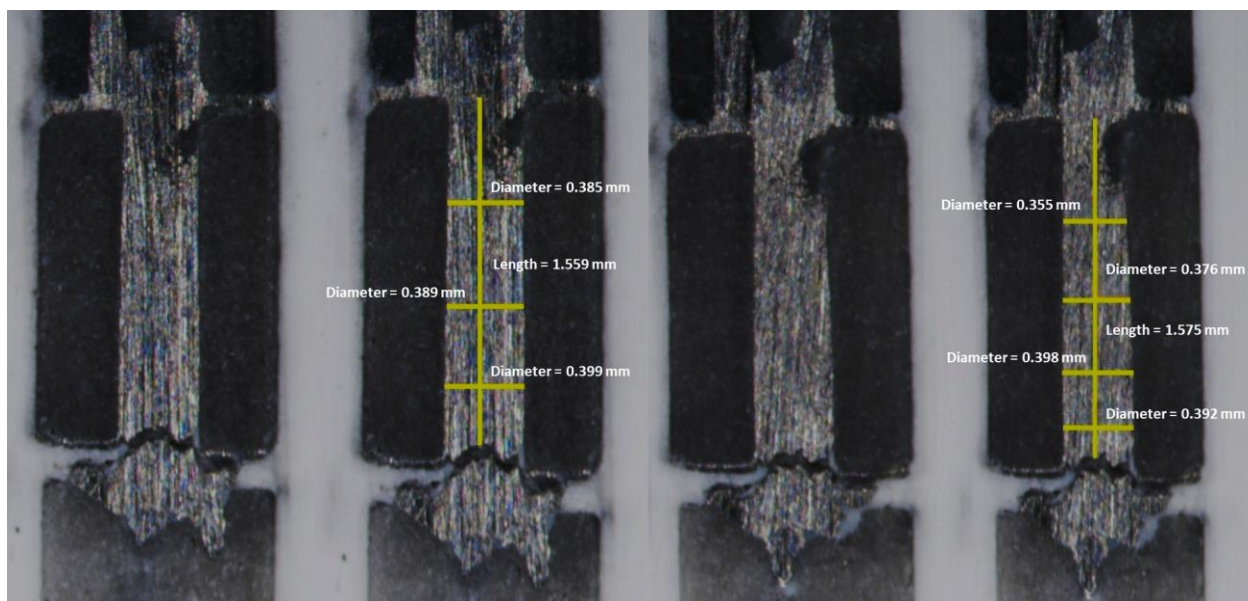


Figure A.1.6: Cross sectional image of the end polishing stage of Fe-5 wt% Ni recovered from 3 GPa and 1960 K.

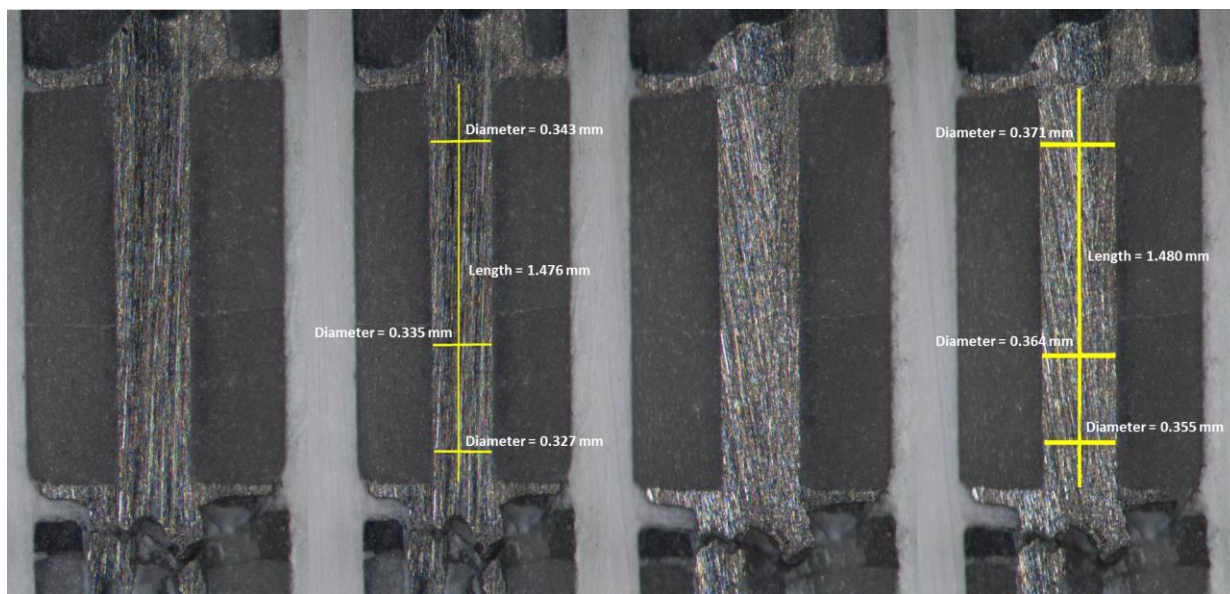


Figure A.1.7: Cross sectional image of the initial polishing stage of Fe-5 wt% Ni recovered from 4 GPa and 1982 K.

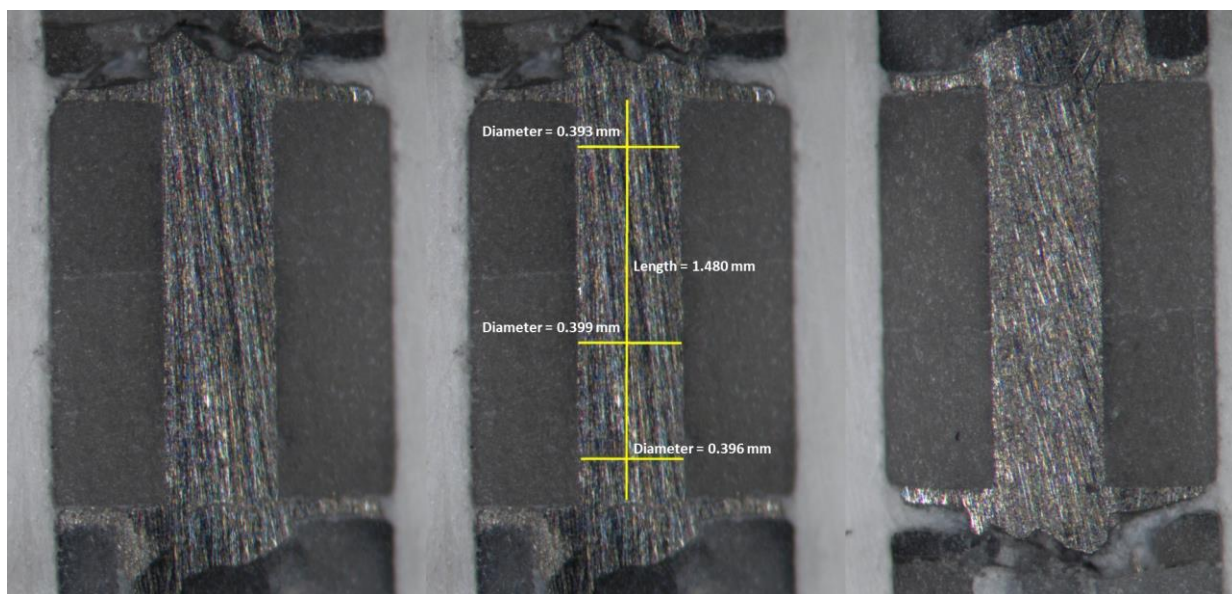


Figure A.1.8: Cross sectional image of the middle polishing stage of Fe-5 wt% Ni recovered from 4 GPa and 1982 K.

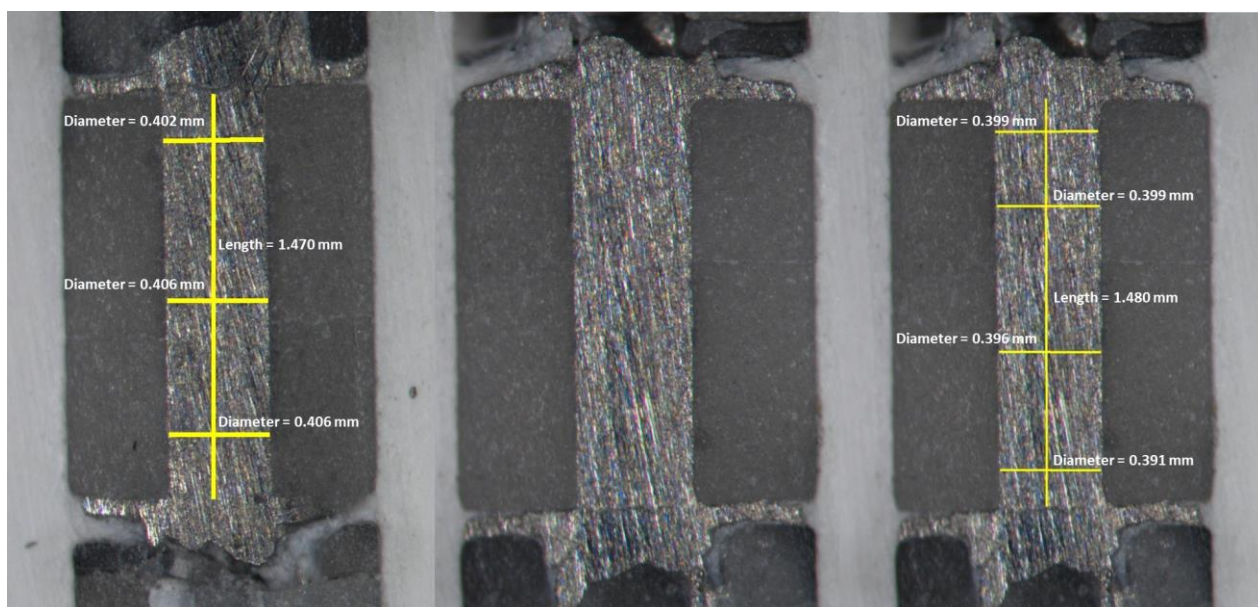


Figure A.1.9: Cross sectional image of the end polishing stage of Fe-5 wt% Ni recovered from 4 GPa and 1982 K.

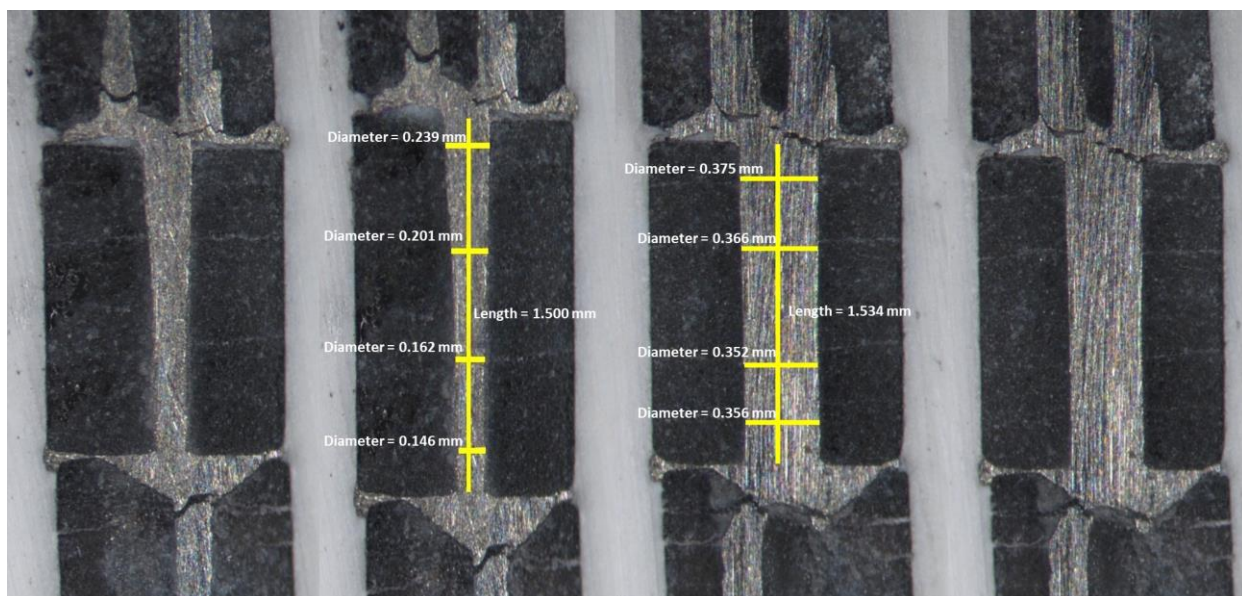


Figure A.1.10: Cross sectional image of the initial polishing stage of Fe-5 wt% Ni recovered from 5 GPa and 2077 K.

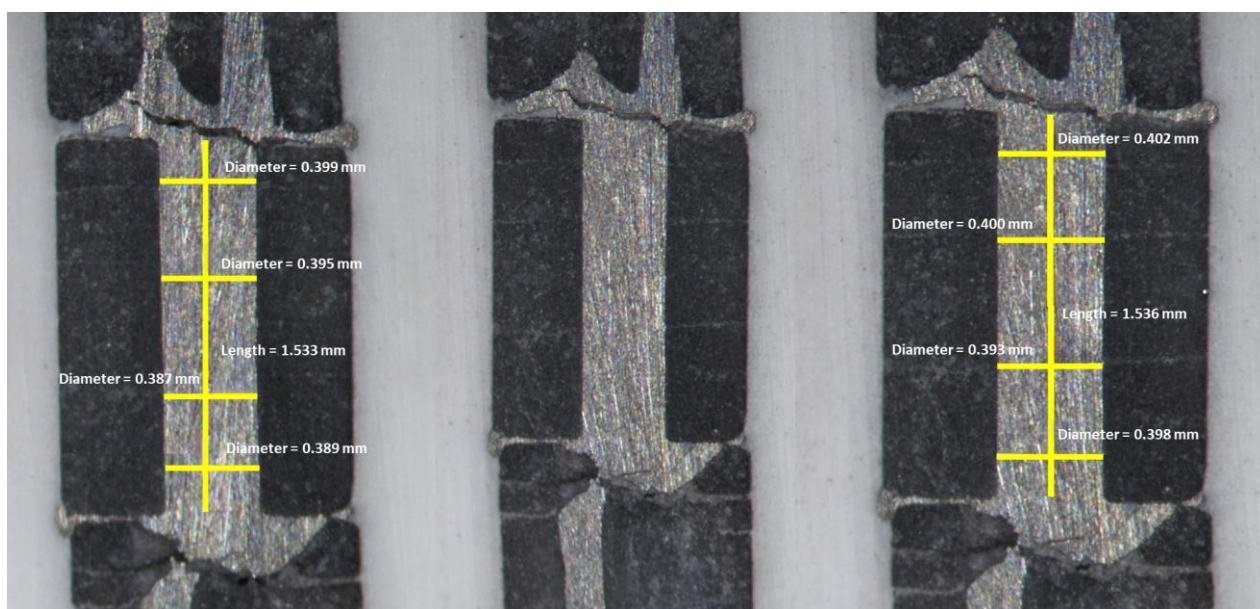


Figure A.1.11: Cross sectional image of the middle polishing stage of Fe-5 wt% Ni recovered from 5 GPa and 2077 K.

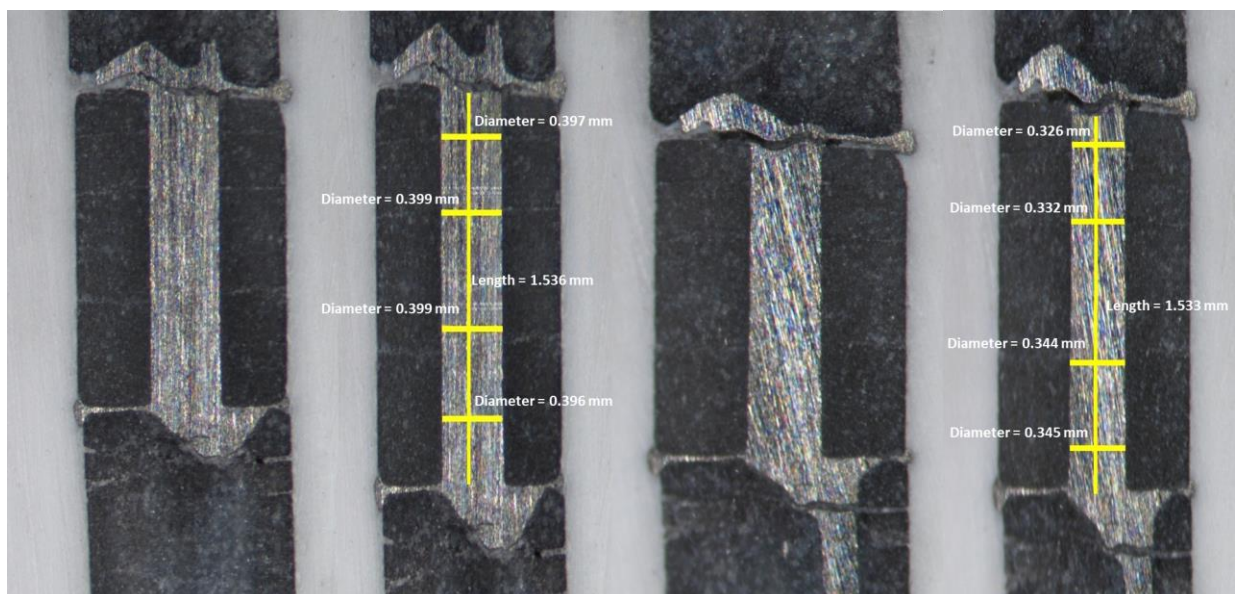


Figure A.1.12: Cross sectional image of the end polishing stage of Fe-5 wt% Ni recovered from 5 GPa and 2077 K.

A.2 EMPA Results

Figure A.2.1 depicts a labeled diagram showcasing the specific location of each target spot on the sample retrieved at 4 GPa and 1986 K.

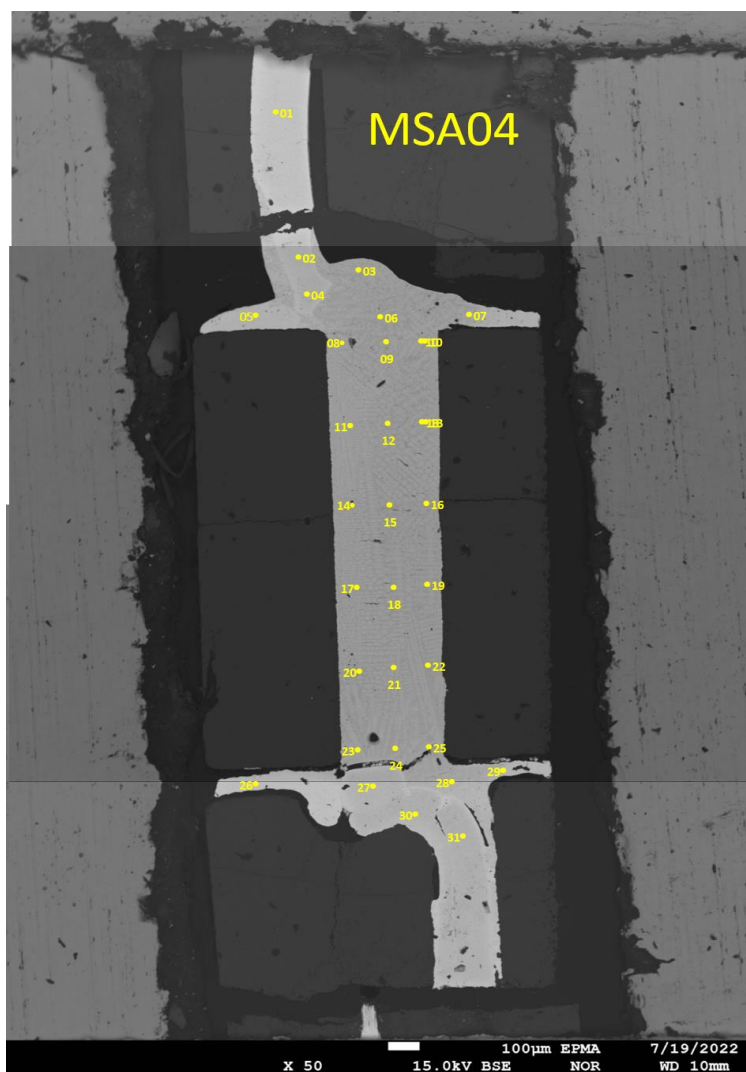


Figure A.2.1: Annotated diagram of the locations of target spots on the sample recovered from 4 GPa and 1982 K.

The table below provides a summary of the mineral composition of each target spot on the sample recovered at 4 GPa and 1982 K. The highlighted part of the table shows the target spots that indicate the outline of the recovered sample.

Table A.2.1: Summary of the mineral composition of each target spot on the sample recovered at 4 GPa and 1982 K.

Comment	Fe	Ni	Pt	Re	W	Total
	(Mass%)	(Mass%)	(Mass%)	(Mass%)	(Mass%)	(Mass%)
01	nd	0.506	0.897	24.186	70.802	96.391
02	nd	nd	1.330	24.510	70.913	96.753
03	32.517	1.908	35.359	2.677	26.041	98.502
04	bdl	bdl	1.013	23.878	71.232	96.123
05	9.088	bdl	85.099	bdl	2.611	96.798
06	35.368	2.165	38.422	2.403	19.959	98.317
07	19.525	1.007	61.377	3.678	12.527	98.114
08	28.677	1.549	34.940	4.804	28.306	98.276
09	32.002	1.781	40.478	2.679	20.572	97.512
10	33.972	1.994	43.510	2.620	16.136	98.232
11	29.035	1.589	37.578	4.393	26.141	98.736
12	37.278	2.197	41.956	2.453	14.855	98.739
13	31.524	1.463	46.981	4.011	14.140	98.119
14	33.213	1.919	39.389	3.282	19.915	97.718
15	34.548	1.788	44.138	3.307	14.043	97.824
16	35.403	1.798	42.768	3.182	13.393	96.544
17	34.510	1.935	40.006	3.054	18.577	98.082
18	34.588	1.760	43.389	3.130	14.908	97.775
19	35.306	1.685	43.650	3.332	14.196	98.169
20	32.129	1.652	42.845	3.651	17.514	97.791
21	33.112	1.720	42.957	3.349	16.905	98.043
22	37.633	2.237	39.917	2.635	14.903	97.325
23	24.590	1.135	56.916	3.860	11.934	98.435
24	27.494	1.360	56.721	2.689	9.494	97.758
25	31.869	1.722	51.762	2.226	9.173	96.752
26	bdl	nd	96.796	nd	nd	96.796
27	nd	bdl	1.290	24.029	70.629	95.948
28	21.431	1.001	69.094	1.216	5.883	98.625
29	4.016	nd	93.577	nd	0.515	98.108
30	bdl	0.631	0.914	4.688	89.242	95.475
31	bdl	nd	1.548	4.517	89.298	95.363

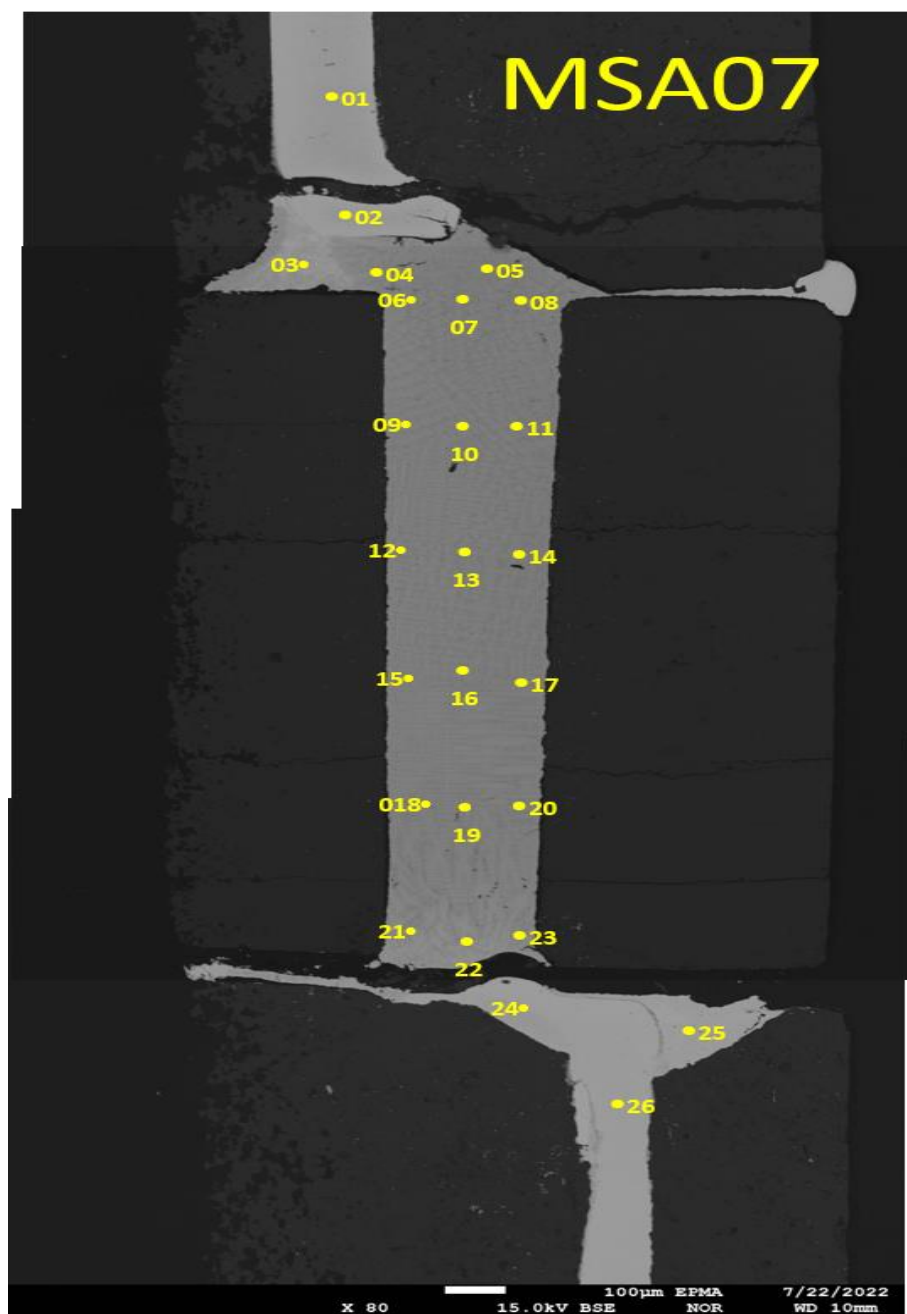


Figure A.2.2: Annotated diagram of the locations of target spots on the sample recovered from 5 GPa and 2077 K.

Table A.2.2: Summary of the mineral composition of each target spot on the sample recovered at 5 GPa and 2077 K.

Comment	Fe	Ni	Pt	Re	W	Total
	(Mass%)	(Mass%)	(Mass%)	(Mass%)	(Mass%)	(Mass%)
01	bdl	0.662	1.431	5.269	90.837	98.199
02	bdl	0.616	1.145	4.993	91.603	98.357
03	17.213	1.011	75.271	0.500	4.971	98.966
04	32.947	1.756	35.412	3.609	24.592	98.316
05	44.244	2.386	34.049	3.167	15.677	99.523
06	43.356	2.375	32.439	2.882	17.160	98.212
07	44.039	2.310	33.856	3.363	15.184	98.752
08	39.990	1.951	35.196	3.663	17.559	98.359
09	42.715	2.322	32.469	3.543	17.507	98.556
10	43.781	2.356	34.208	3.385	15.789	99.519
11	45.263	2.411	34.327	3.494	14.159	99.654
12	42.944	2.464	32.700	3.652	17.737	99.497
13	43.540	2.442	32.425	3.849	16.978	99.234
14	42.998	2.211	34.747	4.170	14.929	99.055
15	41.228	2.262	36.464	3.335	15.472	98.761
16	39.721	2.008	37.247	4.637	15.652	99.265
17	44.535	2.554	34.118	3.159	14.591	98.957
18	40.425	2.133	39.927	3.124	13.586	99.195
19	44.029	2.562	35.831	2.669	14.478	99.569
20	43.418	2.461	34.958	3.327	14.711	98.875
21	28.090	1.475	48.813	4.901	15.748	99.027
22	20.459	0.984	44.816	9.420	24.314	99.993
23	28.362	1.430	39.153	8.445	21.321	98.711
24	bdl	0.643	1.253	11.076	87.120	100.092
25	7.453	0.447	89.066	0.416	1.568	98.950
26	nd	nd	0.867	25.172	73.701	99.740

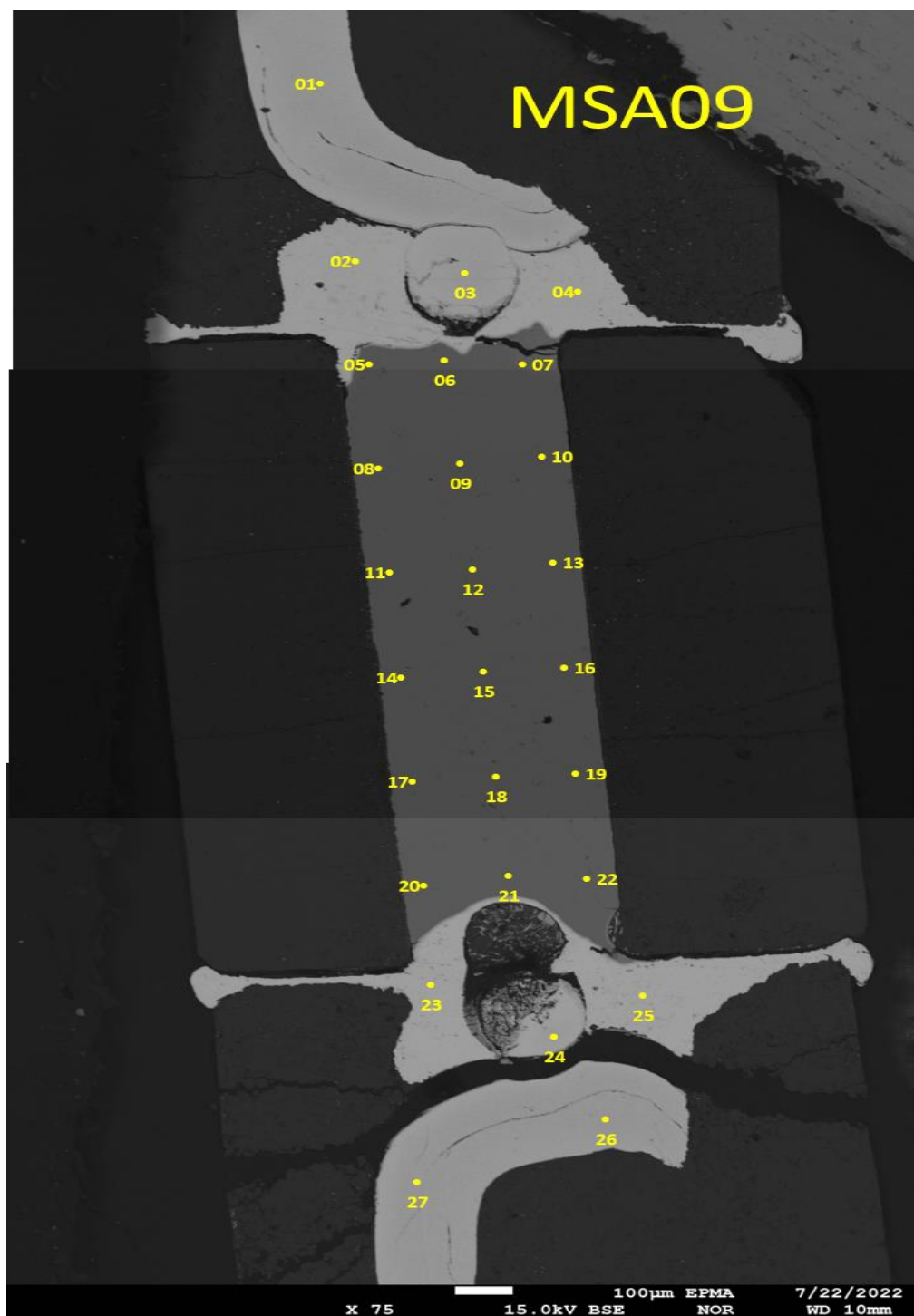


Figure A.2.3: Annotated diagram of the locations of target spots on the sample recovered from 4 GPa and 1723 K.

Table A.2.3: Summary of the mineral composition of each target spot on the sample recovered at 4 GPa and 1723 K.

Comment	Fe	Ni	Pt	Re	W	Total
	(Mass%)	(Mass%)	(Mass%)	(Mass%)	(Mass%)	(Mass%)
01	nd	0.678	1.134	4.888	91.254	97.954
02	nd	nd	96.164	bdl	bdl	96.164
03	bdl	nd	99.321	nd	bdl	99.321
04	bdl	nd	98.175	nd	bdl	98.175
05	94.383	4.872	0.372	nd	bdl	99.627
06	94.538	4.897	0.495	nd	nd	99.930
07	89.680	5.212	3.754	nd	0.640	99.286
08	94.589	5.007	0.440	nd	bdl	100.036
09	94.098	4.919	0.250	nd	nd	99.267
10	94.578	4.825	bdl	nd	bdl	99.403
11	94.139	4.903	0.610	nd	bdl	99.652
12	94.397	4.915	0.574	nd	bdl	99.886
13	94.194	4.890	0.562	nd	bdl	99.646
14	94.562	4.860	0.412	bdl	nd	99.834
15	94.008	4.934	0.270	nd	nd	99.212
16	94.407	4.892	0.496	nd	nd	99.795
17	94.864	4.900	0.410	nd	nd	100.174
18	94.062	4.980	0.473	nd	nd	99.515
19	94.327	4.934	0.315	nd	nd	99.576
20	95.071	4.948	0.281	nd	nd	100.300
21	94.659	4.924	0.345	nd	bdl	99.928
22	94.350	4.928	0.370	nd	bdl	99.648
23	nd	nd	99.138	nd	bdl	99.138
24	nd	0.523	0.911	24.350	72.818	98.602
25	bdl	nd	97.624	nd	bdl	97.624
26	bdl	0.670	1.442	4.709	91.159	97.980
27	nd	0.669	1.253	4.858	91.727	98.507

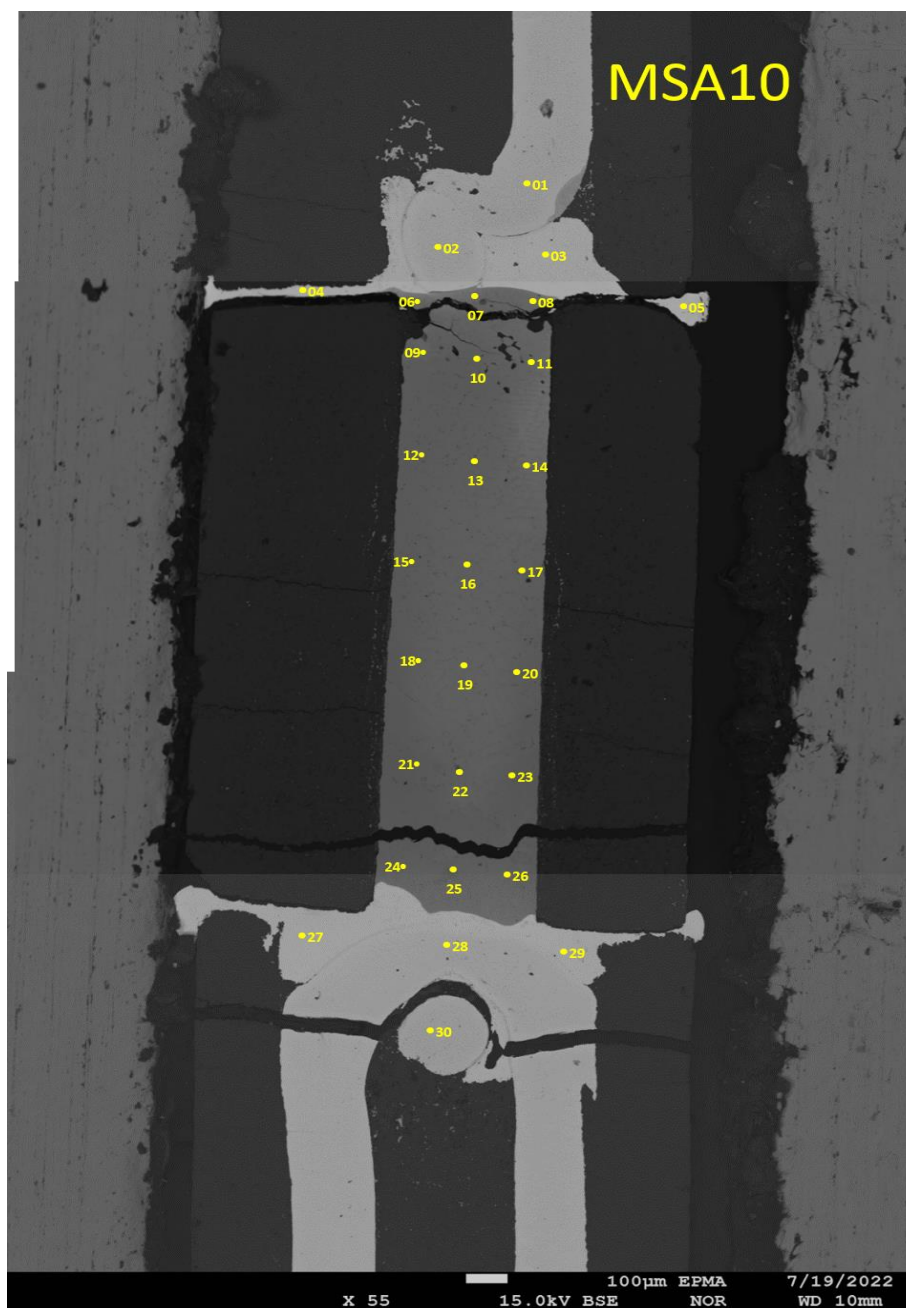


Figure A.2.4: Annotated diagram of the locations of target spots on the sample recovered from 4 GPa and 1847 K.

Table A.2.4: Summary of the mineral composition of each target spot on the sample recovered at 4 GPa and 1847 K.

Comment	Fe	Ni	Pt	Re	W	Total
	(Mass%)	(Mass%)	(Mass%)	(Mass%)	(Mass%)	(Mass%)
01	nd	0.689	0.847	4.725	91.605	97.866
02	nd	0.513	1.352	24.481	71.936	98.282
03	nd	bdl	98.731	nd	bdl	98.731
04	bdl	nd	96.753	nd	bdl	96.753
05	bdl	bdl	95.009	nd	bdl	95.009
06	75.883	3.884	17.727	0.609	2.230	100.333
07	76.641	4.227	9.655	1.840	6.623	98.986
08	77.604	4.085	15.749	nd	0.855	98.293
09	85.959	4.705	8.259	nd	0.309	99.232
10	87.985	4.847	5.797	nd	0.165	98.794
11	79.260	4.208	14.695	bdl	0.529	98.692
12	90.526	4.637	4.473	nd	0.200	99.836
13	87.819	4.873	6.785	bdl	0.266	99.743
14	77.075	3.982	18.176	bdl	0.328	99.561
15	88.464	5.210	4.833	bdl	0.110	98.617
16	84.584	4.354	10.280	nd	0.283	99.501
17	85.647	4.388	9.165	bdl	0.209	99.409
18	91.118	4.547	3.887	nd	bdl	99.552
19	83.694	4.270	10.994	nd	0.352	99.310
20	89.962	4.497	5.305	nd	0.195	99.959
21	94.474	4.467	1.192	nd	bdl	100.133
22	86.390	4.742	8.616	nd	0.477	100.225
23	93.678	4.575	1.502	nd	bdl	99.755
24	85.460	4.536	8.351	nd	bdl	98.347
25	79.238	3.992	15.536	nd	bdl	98.766
26	83.535	4.471	10.934	nd	bdl	98.940
27	nd	nd	100.288	bdl	nd	100.288
28	bdl	0.528	1.118	24.592	72.058	98.296
29	nd	nd	99.629	nd	bdl	99.629
30	nd	nd	0.842	4.661	91.629	97.132

Curriculum Vitae

Name:	Oluwasanmi Orole
Post-secondary Education and Degrees:	<p>Landmark University Omu-aran, Kwara State, Nigeria 2014-2018 B.S.</p> <p>The University of Western Ontario London, Ontario, Canada 2019-2020 Course-based M.Sc., Geophysics</p> <p>The University of Western Ontario London, Ontario, Canada 2021-2023 Thesis-based M.Sc., Geophysics</p>
Honours and Awards:	<p>KEGS Foundation Scholarship Award 2022-2023</p>
Related Work Experience	<p>Teaching Assistant The University of Western Ontario 2021-2023</p>

Publications:

Orole, O. A., Yong, W., & Secco, R. A. (2022). Thermal Convection in Vesta's Core from Experimentally Based Conductive Heat Flow Estimates. *Crystals*, 12(12), 1752. <https://doi.org/10.3390/cryst12121752>.